

Quasinormal Modes, Grebody Factors, and Hawking Radiation Sparsity of Black Holes Influenced by a Global Monopole Charge in Kalb-Ramond Gravity

A. Baruah^a Y. Sekhmani^{b,c} S. K. Maurya^d A. Deshamukhya^a M. K. Jasim^d

^aDepartment of Physics, Albert Einstein School of Physical Sciences, Assam University, Silchar - 788011, Assam, India

^bCenter for Theoretical Physics, Khazar University, 41 Mehseti Street, Baku, AZ1096, Azerbaijan.

^cCentre for Research Impact & Outcome, Chitkara University Institute of Engineering and Technology, Chitkara University, Rajpura, 140401, Punjab, India

^dDepartment of Mathematical and Physical Sciences, College of Arts and Sciences, University of Nizwa, Nizwa 616, Sultanate of Oman

E-mail: anshuman.baruah@aus.ac.in, sekhmaniyassine@gmail.com,
sunil@unizwa.edu.om, atri.deshamukhya@aus.ac.in,
mahmoodkhalid@unizwa.edu.com

Abstract. Kalb-Ramond (KR) gravity is an intriguing model incorporating local Lorentz violation, and black hole (BH) solutions are known to exist. In this study, we investigate some crucial aspects of BHs endowed with a global monopole charge in the self-interacting KR field. Specifically, we study the quasinormal modes (QNMs) corresponding to scalar, electromagnetic, and gravitational perturbations; derive rigorous bounds for the greybody factors (GBFs); and examine the sparsity of Hawking radiation. The effects of the model parameters ℓ (Lorentz-violating parameter in KR gravity) and η (monopole charge) on these phenomena are elaborated. First, QNMs are evaluated with high precision using the 13th-order Padé-averaged WKB method and cross-examined via time-domain analyses within an acceptable parameter space. The results show that the estimated QNMs are more sensitive to ℓ ; however, both model parameters influence the frequency spectra. The derived bounds on the GBFs aid in further constraining the parameter space. It is shown that ℓ and η have a similar effect on the greybody bounds. Furthermore, positive and negative values of ℓ have opposing effects in that the bounds are reversed for the two cases. The analyses of the Hawking radiation sparsity highlight the effect of ℓ , and two scenarios are noted: either the radiation emitted is less sparse than Hawking radiation, or it is more sparse during the evaporation phase. Thus, this work presents a comprehensive account of BHs in KR gravity with a global monopole charge.

Contents

1	Introduction	1
2	Black Hole in KR Gravity with a Global Monopole Charge	3
3	Quasinormal Modes	4
3.1	The Padé-averaged WKB method for QNMs	4
3.2	Massless Scalar Perturbations	5
3.2.1	Variation of scalar QNMs with ℓ	6
3.2.2	Variation of scalar QNMs with η	7
3.3	Electromagnetic Perturbations	10
3.3.1	Variation of EM QNMs with ℓ	11
3.3.2	Variation of EM QNMs with η	12
3.4	Gravitational Perturbations	13
3.4.1	Variation of gravitational QNMs with ℓ	16
3.4.2	Variation of gravitational QNMs with η	17
3.5	Time-domain QNMs	18
3.6	Frequency extraction using the Prony method	21
4	Greybody Factors and Sparsity of Hawking Radiation	22
4.1	Greybody Factors	22
4.2	Sparsity of Hawking Radiation	27
5	Discussions	29

1 Introduction

General Relativity (GR) is a well-tested theory that has withstood over a century of tests, ranging from the perihelion precession of Mercury to the detection of gravitational waves (GWs) and imaging of black hole (BH) shadows. However, GR has inherent limitations in that it cannot account for the dark sector of the universe and is a completely classical theory. Various modifications and/or extensions to GR have been proposed over the decades to address these limitations, and recent progress in observational astrophysics has opened the potential to explore deviations from GR. To this end, BHs serve as an intriguing testing ground. Stemming from the first reported solution to the field equations of GR in 1916, BHs are extremely compact objects formed during stellar collapse, at the cores of galaxies, and possibly due to density fluctuations in the early universe. Although state-of-the-art observations of BHs, such as those by the LIGO-Virgo-KAGRA and EHT collaborations, agree with GR [1–4], strong motivations exist that hint at the possible detection of deviations at higher sensitivities. It is anticipated that such observations may be realized by planned missions such as the Cosmic Explorer, Einstein Telescope, Lisa Telescope, Tian Chen, Taiji, etc. In addition, studies on GWs and optical properties of BHs in modifications of GR is a subject of considerable interest.

Symmetries are of fundamental importance to physics, and Lorentz symmetry ensures that physical laws remain consistent across inertial frames of reference. However, theoretical

evidence suggests that Lorentz symmetry may be violated at extremely high energies and/or small length scales [5–13]. Such models of gravity contain variables/parameters that lead to Lorentz symmetry breaking (LSB) either explicitly or spontaneously. On the one hand, explicit violations are observed when the effective action contains functions of fixed vector or tensor fields that define a preferred direction or frame (the Lagrangian breaks Lorentz symmetry). On the other hand, spontaneous violations are observed when the vacuum expectation value (VEV) of a dynamical field breaks Lorentz symmetry. Thus, it is important to constrain such model parameters to ensure precision of future observations that may hint at the exact $4D$ theory of gravity. To this end, the Standard Model Extension (SME) framework is a well-studied paradigm for spontaneous LSB; SME includes a vector field called the bumblebee field [14] with a non-zero VEV. BH and wormhole solutions in bumblebee gravity have been studied extensively in literature [15–26]. Here, we focus instead on a higher-rank field of interest.

In addition to the bumblebee field, a rank-two antisymmetric field, called the Kalb-Ramond (KR) field, has been studied extensively [27, 28]. Stemming from bosonic string theory, the non-minimal coupling of the KR field with gravity endows it with a non-zero VEV, leading to spontaneous, local LSB. The KR field may be interpreted as a generalization of the electromagnetic potential with two indices. It is well known that p -form theories [29] are generalizations of Maxwell’s electrodynamics, with the gauge potential being a higher-rank differential form [30]. In the KR model, the 2-form potential and field strength are given as $B_2 = \frac{1}{2}B_{\mu\nu}dx^\mu \wedge dx^\nu$ and $H_{\alpha\mu\nu} = \partial_{[\alpha}B_{\mu\nu]}$, respectively. The KR field has been studied in the context of BH physics [31–33], braneworld scenarios [34], cosmology [35, 36], etc. Static, spherically-symmetric BH in KR gravity have been reported [37], and relevant properties such as quasinormal modes (QNMs), light deflection, and particle dynamics have been studied [38–41]. An intriguing new solution in KR gravity has been reported very recently by Fathi and Ovgün [42], where they consider the interaction of the KR field with a global monopole charge. Global monopoles are topological defects arising from the spontaneous breaking of global symmetries, specifically, $O(3) \rightarrow U(1)$ symmetry breaking, in the context of early-universe phase transitions [43–45]. They have significant implications both for cosmology and BH astrophysics. Global monopoles are generally associated with physical singularities; however, their pathological behaviors can be ameliorated when gravitational effects are taken into consideration [46]. Especially, the self-energy divergence issue is resolved, highlighting its potential physical significance in astrophysical contexts [47].

In this study, we study some properties of the BH with a global monopole charge in KR gravity. Specifically, we study the QNMs, which are characteristic responses of BHs to perturbations using a high-accuracy method. Next, we derive strict bounds on the grey-body factors (GBFs), which are crucial thermodynamic parameters concerning the radiative spectra of BHs. Finally, we examine the sparsity of Hawking radiation emitted from the BH.

The remainder of this paper is organized as follows. In Section 2, we review KR gravity in the context of its interaction with a global monopole and present the BH solution of interest. In Section 3, we study the QNMs of the BH. In Section 4.1, we derive rigorous bounds on the GBFs. In Section 4.2, we discuss the sparsity of Hawking radiation of the KR BH, and finally, in Section 5, we present some discussions and conclude the paper.

Throughout the work, we paper in the natural system of units ($\kappa = 8\pi G = c = \hbar = 1$) and the $(-, +, +, +)$ sign convention.

2 Black Hole in KR Gravity with a Global Monopole Charge

The Einstein-Hilbert action minimally coupled with the self-interacting KR field is given by [28, 37]

$$S = \frac{1}{2} \int d^4x \sqrt{-g} \left[R - \frac{1}{6} H^{\mu\nu\rho} H_{\mu\nu\rho} - V(B_{\mu\nu} B^{\mu\nu}) + \xi_2 B^{\rho\mu} B_\mu^\nu R_{\rho\nu} + \xi_3 B^{\mu\nu} B_{\mu\nu} R \right] + \int d^4x \sqrt{-g} \mathcal{L}_M, \quad (2.1)$$

where ξ_i represent the coupling constants. The field of interest here is the antisymmetric 2-tensor (KR field) $B_{\mu\nu} = -B_{\nu\mu}$, with its dual given by $\mathfrak{B}_{\mu\nu} \equiv \frac{1}{2} \epsilon_{\mu\nu\kappa\lambda} B^{\kappa\lambda}$, where $\epsilon_{\mu\nu\kappa\lambda}$ is the completely antisymmetric Levi-Civita tensor. Next, the field strength is given by the completely antisymmetric field-strength tensor defined in terms of derivatives of $B_{\mu\nu}$ as $H_{\lambda\mu\nu} = \partial_\lambda B_{\mu\nu} + \partial_\mu B_{\nu\lambda} + \partial_\nu B_{\lambda\mu}$. This can be interpreted as components of an exact 3-form field H (the pseudoscalar axion) constructed from exterior derivatives of the 2-form B [27, 28]. Moreover, \mathcal{L}_m denotes the matter Lagrangian corresponding to a global monopole, defined as [46]:

$$\mathcal{L}_m = \frac{1}{2} \partial_\mu \varphi^a \partial^\mu \varphi^a - \frac{\lambda}{4} (\varphi^a \varphi^a - \eta^2)^2 \quad (2.2)$$

Here, λ is a coupling constant and η is the monopole charge. Equation (2.1) can be varied with respect to $g^{\mu\nu}$ to obtain the gravitational field equation as:

$$R_{\mu\nu} - \frac{1}{2} g_{\mu\nu} R = T_{\mu\nu}^M + T_{\mu\nu}^{KR} \quad (2.3)$$

Considering a non-vanishing VEV for the KR field ($\langle B_{\mu\nu} \rangle = b_{\mu\nu}$), the potential should be of the form $V = V(B^{\mu\nu} B_{\mu\nu} \pm b^2)$, using which the field equations becomes:

$$R_{\mu\nu} = T_{\mu\nu}^M - \frac{1}{2} g_{\mu\nu} T^M + V'(Y) + \xi_2 \left[g_{\mu\nu} b^{\alpha\gamma} b_\gamma^\beta R_{\alpha\beta} - b^{\alpha\beta} b_{\mu\beta} R_{\nu\alpha} - b^{\alpha\beta} b_{\nu\beta} R_{\mu\alpha} \right. \\ \left. + \frac{1}{2} \nabla_\alpha \nabla_\mu (b^{\alpha\beta} b_{\nu\beta}) + \frac{1}{2} \nabla_\alpha \nabla_\nu (b^{\alpha\beta} b_{\mu\beta}) - \frac{1}{2} \square (b_\mu{}^\gamma b_{\nu\gamma}) \right] \quad (2.4)$$

with $T^M = g^{\mu\nu} T_{\mu\nu}^M$ and $Y = 2b_{\mu\alpha} b_\nu{}^\alpha + b^2 g_{\mu\nu}$. Moreover, the energy-momentum tensor corresponding to \mathcal{L}_M is given by

$$T_{\mu\nu}^M = \partial_\mu \varphi^a \partial_\nu \varphi^a - g_{\mu\nu} \left[\frac{1}{2} \partial^\rho \varphi^a \partial_\rho \varphi^a - \frac{\lambda}{4} (\varphi^a \varphi^a - \eta^2)^2 \right]. \quad (2.5)$$

Using the static, spherically-symmetric metric ansatz

$$ds^2 = -A(r) dt^2 + B(r) dr^2 + r^2 d\theta^2 + r^2 \sin^2 \theta d\phi^2, \quad (2.6)$$

the following field equations are obtained

$$\frac{2A''(r)}{A(r)} - \frac{A'(r)B'(r)}{A(r)B(r)} - \frac{A'(r)^2}{A(r)^2} + \frac{4}{r} \frac{A'(r)}{A(r)} = 0 \quad (2.7)$$

$$\frac{2A''(r)}{A(r)} - \frac{A'(r)B'(r)}{A(r)B(r)} - \frac{A'(r)^2}{A(r)^2} - \frac{4}{r} \frac{B'(r)}{B(r)} = 0 \quad (2.8)$$

$$\begin{aligned} \frac{2A''(r)}{A(r)} - \frac{A'(r)B'(r)}{A(r)B(r)} - \frac{A'(r)^2}{A(r)^2} + \frac{1+\ell}{\ell r} \left[\frac{A'(r)}{A(r)} - \frac{B'(r)}{B(r)} \right] \\ - [1 - b^2 r^2 V'(Y)] \frac{2B(r)}{\ell r^2} + \frac{2(1-\ell)}{\ell r^2} + \eta^2 = 0 \end{aligned} \quad (2.9)$$

with $\ell \equiv \xi_2 b^2/2$. Considering the VEV at the local minimum of the potential [48] and subtracting Eq. (8) from (7) leads to $A(r) = B(r)^{-1}$. Finally, subtracting Eq. (9) from (7) provides the solution for $A(r)$, which in the second order of the monopole charge is

$$A(r) = \frac{1}{1-\ell} - \frac{2M}{r} + \frac{\ell M \eta^2 r}{2(1-\ell)} - \frac{\ell \eta^2 r^2}{6(1-\ell)^2} + \mathcal{O}(\eta^4). \quad (2.10)$$

This BH with a global monopole charge has been studied in terms of the horizon properties, thermodynamics, and solar system tests, constraining the acceptable ranges of ℓ and η [42]. In the next sections, we study the QNMs, GBFs, and sparsity of Hawking radiation for this BH.

3 Quasinormal Modes

In this section, we study the QNMs of the KR BH with a global monopole charge. QNMs quantify the responses of BHs to perturbations of test fields. It should be noted that the back-reaction of the fields on the space-time is considered negligible in such analyses. We first study the variations of the QNMs corresponding to scalar, electromagnetic (EM), and gravitational perturbations of the KR BH with the model parameters in the frequency domain using the 13th-order Padé-averaged WKB method. Then, we study the time-domain profiles of the perturbations and extract the dominant QNMs for each case. We start with a brief introduction of the Padé-averaged WKB method.

3.1 The Padé-averaged WKB method for QNMs

The WKB method is a well-established approach to solve BH perturbation equations in the frequency domain [49–52]. However, the accuracy of the estimated frequencies degrades for $n \geq l$. To ameliorate this issue, the Padé approximation [53] can be used to evaluate QNMs with higher precision. Here, we use the Padé-averaged WKB approach, as briefly outlined below, to estimate the frequency-domain QNMs for the KR BH subjected to scalar, EM, and gravitational perturbations.

For a wave-like equation

$$\frac{d^2\Psi}{dx^2} = U(x, \omega)\Psi, \quad (3.1)$$

the WKB method yields solutions in asymptotic regions described by a superposition of ingoing and outgoing waves [54]. The asymptotic solutions are matched with the extrema

of the effective potential via a Taylor expansion. The WKB method provides a closed-form formula for the QNM frequencies as [55]

$$\omega^2 = V_0 + A_2(\mathcal{K}^2) + A_4(\mathcal{K}^2) + A_6(\mathcal{K}^2) + \dots - i\mathcal{K}\sqrt{-2V_2} (1 + A_3(\mathcal{K}^2) + A_5(\mathcal{K}^2) + A_7(\mathcal{K}^2) \dots), \quad (3.2)$$

The divergence of the Taylor series is avoided by using Padé approximants [53], where a polynomial $P_k(\epsilon)$, defined in powers of an *order parameter* ϵ , modifies Eq. (3.2) as

$$P_k(\epsilon) = V_0 + A_2(\mathcal{K}^2)\epsilon^2 + A_4(\mathcal{K}^2)\epsilon^4 + A_6(\mathcal{K}^2)\epsilon^6 + \dots - i\mathcal{K}\sqrt{-2V_2} (\epsilon + A_3(\mathcal{K}^2)\epsilon^3 + A_5(\mathcal{K}^2)\epsilon^5 \dots) \quad (3.3)$$

the Padé approximants $P_{\tilde{n}/\tilde{m}}(\epsilon)$ for the polynomial $P_k(\epsilon)$ is given by rational functions [53, 55]:

$$P_{\tilde{n}/\tilde{m}}(\epsilon) = \frac{Q_0 + Q_1\epsilon + \dots + Q_{\tilde{n}}\epsilon^{\tilde{n}}}{R_0 + R_1\epsilon + \dots + R_{\tilde{m}}\epsilon^{\tilde{m}}}, \quad (3.4)$$

with $\tilde{n} + \tilde{m} = k$. To estimate the accuracy of the approach, we calculate the associated errors in the frequencies. In the WKB formula used, corrections in each order affect the real and imaginary parts of the squared frequency, and the error in ω_k for an arbitrary order k can be estimated as

$$\Delta_k = \frac{|\omega_{k+1} - \omega_{k-1}|}{2} \quad (3.5)$$

3.2 Massless Scalar Perturbations

Considering massless scalar perturbations, we start with the Klein–Gordon equation; the perturbed metric can be recast without loss of generality as follows [56]:

$$ds^2 = -|g_{tt}|dt^2 + g_{rr}dr^2 + r^2d\theta^2 + r^2\sin^2\theta(d\phi - adt - bdr - cd\theta)^2 \quad (3.6)$$

Here, a , b , and c are functions of t , r , and θ , encoding the perturbations. We leverage the tetrad formalism and adopt a basis e_a^μ associated with the metric $g_{\mu\nu}$, and satisfying

$$\begin{aligned} e_\mu^{(a)} e_{(b)}^\mu &= \delta_{(b)}^{(a)} \\ e_\mu^{(a)} e_{(a)}^\nu &= \delta_\mu^\nu \\ e_\mu^{(a)} &= g_{\mu\nu} \eta^{(a)(b)} e_{(b)}^\nu \\ g_{\mu\nu} &= \eta_{(a)(b)} e_\mu^{(a)} e_\nu^{(b)} = e_{(a)\mu} e_\nu^{(a)}. \end{aligned} \quad (3.7)$$

In the new basis, vector and tensor quantities are projected as

$$\begin{aligned} P_\mu &= e_\mu^{(a)} P_{(a)}, \\ P_{(a)} &= e_{(a)}^\mu P_\mu, \\ A_{\mu\nu} &= e_\mu^{(a)} e_\nu^{(b)} A_{(a)(b)}, \\ A_{(a)(b)} &= e_{(a)}^\mu e_{(b)}^\nu A_{\mu\nu}. \end{aligned} \quad (3.8)$$

Considering the propagation of a massless scalar field around the black hole and assuming that the reaction of the scalar field on the space-time is negligible, the scalar QNMs can be described by the Klein–Gordon equation given by

$$\square\Phi = \frac{1}{\sqrt{-g}} \partial_\mu (\sqrt{-g} g^{\mu\nu} \partial_\nu \Phi) = 0. \quad (3.9)$$

Neglecting the back-reaction of the field, one can consider Eq. (3.6) only up to the zeroth order:

$$ds^2 = -|g_{tt}|dt^2 + g_{rr}dr^2 + r^2d\Omega_2^2 \quad (3.10)$$

The scalar field can conventionally be decomposed using spherical harmonics as

$$\Phi(t, r, \theta, \phi) = \frac{1}{r} \sum_{l,m} \psi_l(t, r) Y_{lm}(\theta, \phi), \quad (3.11)$$

where $\psi_l(t, r)$ is the time-dependent radial wave function. Further, l and m are the indices of the spherical harmonics Y_{lm} . Then, Eq. (3.9) yields

$$\partial_{r_*}^2 \psi(r_*)_l + \omega^2 \psi(r_*)_l = V_s(r) \psi(r_*)_l, \quad (3.12)$$

where r_* is the tortoise coordinate defined as

$$\frac{dr_*}{dr} = \sqrt{g_{rr} |g_{tt}^{-1}|} \quad (3.13)$$

and $V_s(r)$ is the effective potential of the field given by

$$V_s(r) = |g_{tt}| \left(\frac{l(l+1)}{r^2} + \frac{1}{r \sqrt{|g_{tt}| g_{rr}}} \frac{d}{dr} \sqrt{|g_{tt}| g_{rr}^{-1}} \right). \quad (3.14)$$

The effect of ℓ and η on the scalar potential has been visualized in Fig. 1.

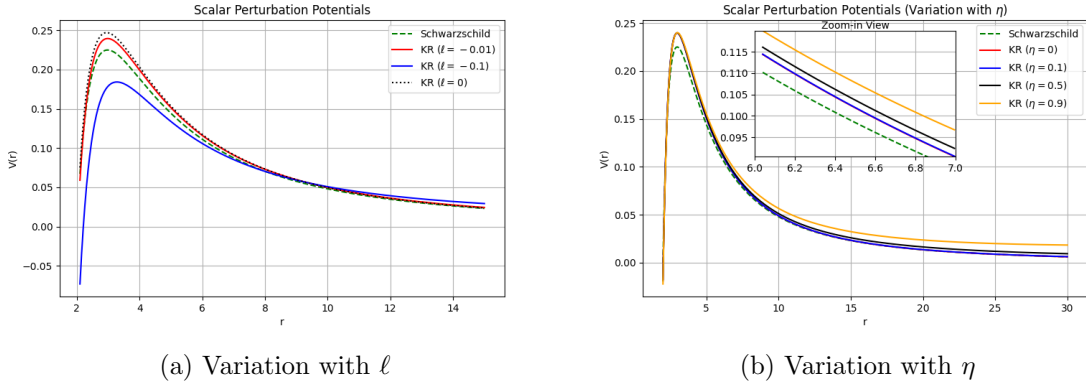


Figure 1: Variation of the scalar potential with ℓ and η .

3.2.1 Variation of scalar QNMs with ℓ

The variation of the scalar QNMs with ℓ is evident from the data listed in Table 1 and visualized in Fig. 2. It can be seen that ω_{Re} exhibits a monotonic increase as ℓ is varied from -0.01 to 0. For example, for $n = 0$ (the fundamental mode), ω_{Re} increases from approximately 0.8545 to 0.8674. Similar increasing trends are seen for higher overtones. The systematic trend in the real part indicates that the oscillation frequency of the QNMs is sensitive to the parameter ℓ in that as ℓ increases (or in our parameterization, becomes less negative), the oscillatory response becomes slightly more rapid. The imaginary part, which is associated with the damping rate of the mode, also exhibits systematic variation. For instance, for the

fundamental mode, ω_{Im} becomes more negative, from approximately -0.09442 to -0.09639 with increasing ℓ . Similar trends are observed for the higher overtones, suggesting that the damping becomes slightly more efficient as ℓ increases. Physically, this indicates that the QNMs decay faster as $\ell \rightarrow 0$. Across all values of ℓ , the modes corresponding to higher overtone numbers exhibit both lower ω_{Re} and more negative ω_{Im} compared to those with lower n . This hierarchical structure is typical in QNM spectra and confirms that the influence of ℓ is modulated by the overtone index. Thus, the oscillatory frequency and damping rate exhibit systematic variations with n . The relative error Δ associated with each frequency has also been computed and visualized in Fig. 3; its logarithmic scaling with ℓ suggests that the numerical uncertainties are small but vary with ℓ . The error estimates confirm that the trends observed in the QNMs are robust over the range of ℓ values considered. The systematic behavior is not an artifact of numerical noise, but reflects actual physical dependence on ℓ . Overall, it can be seen that the 13th-order Padé-averaged WKB method yields accurate results.

ℓ	n	ω	Δ
-0.01	0	$0.854519 - 0.0944194i$	7.03513×10^{-9}
	1	$0.843157 - 0.284922i$	1.96032×10^{-7}
	2	$0.82151 - 0.480279i$	9.31994×10^{-6}
	3	$0.791767 - 0.683183i$	0.000142056
-0.008	0	$0.857073 - 0.0948092i$	7.2419×10^{-9}
	1	$0.845662 - 0.286099i$	2.9498×10^{-7}
	2	$0.823922 - 0.482263i$	9.9095×10^{-6}
	3	$0.79405 - 0.686006i$	0.000156267
-0.006	0	$0.859639 - 0.0952013i$	7.30235×10^{-9}
	1	$0.848179 - 0.287282i$	2.85788×10^{-7}
	2	$0.826347 - 0.484261i$	0.000010104
	3	$0.796348 - 0.688848i$	0.000164913
-0.004	0	$0.862218 - 0.0955957i$	7.86920×10^{-9}
	1	$0.85071 - 0.288473i$	3.80260×10^{-7}
	2	$0.828782 - 0.486269i$	0.0000109012
	3	$0.79865 - 0.691702i$	0.000180047
-0.002	0	$0.86481 - 0.0959925i$	7.30356×10^{-9}
	1	$0.853252 - 0.289671i$	2.07926×10^{-7}
	2	$0.831232 - 0.488294i$	0.0000102581
	3	$0.800732 - 0.694983i$	0.000813118
0	0	$0.867416 - 0.0963917i$	7.53890×10^{-9}
	1	$0.855808 - 0.290876i$	3.13969×10^{-7}
	2	$0.833692 - 0.490326i$	0.0000104755
	3	$0.803307 - 0.6975i$	0.000166087

Table 1: Variation of $l = 4$ scalar QNMs with ℓ and fixed $\eta = 0.3$

3.2.2 Variation of scalar QNMs with η

Next, we analyze the behavior of the scalar QNMs with η while keeping ℓ fixed for four overtone numbers ($n = 0, 1, 2, 3$) over the range $\eta \in [0, 0.9]$. It can be seen that ω_{Re} exhibits

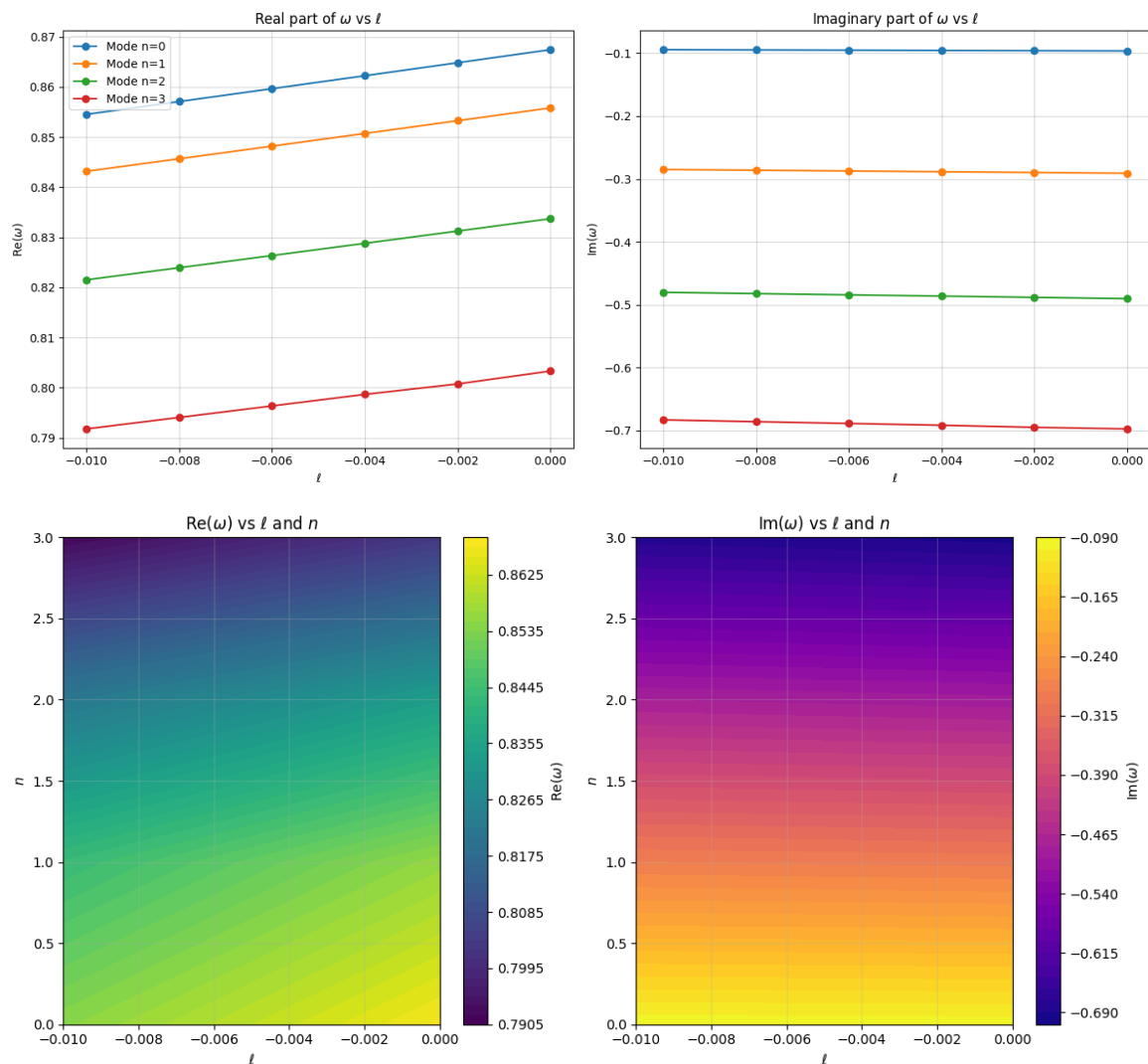


Figure 2: Variation of the $l = 4$ scalar QNMs with l and fixed $\eta = 0.3$.

a slight, monotonic increase with increasing η for each overtone. Although the changes are subtle, typically on the order of 10^{-4} , the trend is consistent across all overtones and possibly, indicative of a weak dependence on η . In contrast, ω_{Im} , exhibits a systematic decrease in its absolute magnitude with increasing η . Physically, this reduction in $|\omega_{\text{Im}}|$ implies that the damping reduces (or equivalently, decay time increases) with increasing η . This behavior may be indicative of a weakening of the dissipative effects in the system. Moreover, for the lower modes ($n = 0$ and $n = 1$), the errors remain consistently small (on the order of 10^{-9} and 10^{-7} , respectively) across the studied range of η . However, for the higher overtones ($n = 2$ and $n = 3$), notable deviations at specific values of η are observed. In particular, an anomalous increase in the error for the $n = 2$ mode at $\eta \approx 0.5$ and for the $n = 3$ mode near $\eta \approx 0.7$ suggests increased sensitivity of the WKB method.

η	n	ω	Δ
0	0	$0.8545 - 0.0944908i$	7.08669×10^{-9}
	1	$0.843174 - 0.285124i$	2.91345×10^{-7}
	2	$0.821584 - 0.480579i$	0.000010025
	3	$0.791894 - 0.683541i$	0.000160666
0.1	0	$0.854502 - 0.0944829i$	7.03077×10^{-9}
	1	$0.843172 - 0.285102i$	2.061503×10^{-7}
	2	$0.821576 - 0.480547i$	9.83541×10^{-6}
	3	$0.791882 - 0.683507i$	0.000154594
0.2	0	$0.854508 - 0.0944591i$	7.06444×10^{-9}
	1	$0.843166 - 0.285034i$	2.71866×10^{-7}
	2	$0.821551 - 0.480445i$	9.76061×10^{-6}
	3	$0.791836 - 0.68338i$	0.000154112
0.3	0	$0.854519 - 0.0944194i$	7.03512×10^{-9}
	1	$0.843157 - 0.284922i$	1.96032×10^{-7}
	2	$0.82151 - 0.480279i$	9.31993×10^{-6}
	3	$0.791767 - 0.683183i$	0.000142056
0.4	0	$0.854535 - 0.0943638i$	7.10626×10^{-9}
	1	$0.843144 - 0.284765i$	1.47834×10^{-7}
	2	$0.821452 - 0.480043i$	9.67111×10^{-6}
	3	$0.791665 - 0.682886i$	0.00015724
0.5	0	$0.854557 - 0.0942922i$	7.78794×10^{-9}
	1	$0.843128 - 0.284563i$	3.59920×10^{-7}
	2	$0.821696 - 0.47965i$	0.000668629
	3	$0.791528 - 0.682512i$	0.000162645
0.6	0	$0.854585 - 0.0942048i$	2.31978×10^{-8}
	1	$0.843111 - 0.284316i$	7.11556×10^{-8}
	2	$0.82129 - 0.479375i$	8.70463×10^{-6}
	3	$0.791376 - 0.68208i$	0.000139143
0.7	0	$0.854622 - 0.0941012i$	7.07419×10^{-9}
	1	$0.843092 - 0.284024i$	2.47424×10^{-7}
	2	$0.821185 - 0.478938i$	9.307742×10^{-6}
	3	$0.790512 - 0.682186i$	0.00176716
0.8	0	$0.854666 - 0.0939816i$	6.38668×10^{-9}
	1	$0.843073 - 0.283687i$	8.82210×10^{-8}
	2	$0.821069 - 0.47844i$	9.04664×10^{-6}
	3	$0.790982 - 0.680945i$	0.000144749
0.9	0	$0.854721 - 0.0938459i$	7.16993×10^{-9}
	1	$0.843055 - 0.283305i$	1.63755×10^{-7}
	2	$0.820935 - 0.477872i$	8.39504×10^{-6}
	3	$0.790726 - 0.680256i$	0.000134466

Table 2: Variation of $l = 4$ scalar QNMs with η and fixed $\ell = -0.01$



Figure 3: Errors in Table 1

3.3 Electromagnetic Perturbations

Here, we consider electromagnetic (EM) perturbations on the KR BH in the tetrad formalism [57]. Using the Bianchi identity of the EM field strength $F_{[a(b)c]} = 0$, we have:

$$\left(r\sqrt{|g_{tt}|} F_{(t)(\phi)} \right)_{,r} + r\sqrt{g_{rr}} F_{(\phi)(r),t} = 0, \quad (3.15)$$

$$\left(r\sqrt{|g_{tt}|} F_{(t)(\phi)} \sin \theta \right)_{,\theta} + r^2 \sin \theta F_{(\phi)(r),t} = 0. \quad (3.16)$$

The conservation equation, $\eta^{(b)(c)}(F_{(a)(b)})_{|c)} = 0$, gives

$$\left(r\sqrt{|g_{tt}|} F_{(\phi)(r)} \right)_{,r} + \sqrt{|g_{tt}|g_{rr}} F_{(\phi)(\theta),\theta} + r\sqrt{g_{rr}} F_{(t)(\phi),t} = 0. \quad (3.17)$$

Redefining the field perturbation as $\mathcal{F} = F_{(t)(\phi)} \sin \theta$, Eq. (3.17) can be differentiated and used in Eqs. (3.15) and (3.16) to obtain

$$\left[\sqrt{|g_{tt}|g_{rr}^{-1}} \left(r\sqrt{|g_{tt}|} \mathcal{F} \right)_{,r} \right]_{,r} + \frac{|g_{tt}|\sqrt{g_{rr}}}{r} \left(\frac{\mathcal{F}_{,\theta}}{\sin \theta} \right)_{,\theta} - r\sqrt{g_{rr}} \mathcal{F}_{,tt} = 0, \quad (3.18)$$

Then, using the Fourier and field decompositions, $(\partial_t \rightarrow -i\omega)$ and $\mathcal{F}(r, \theta) = \mathcal{F}(r)Y_{\theta}/\sin \theta$, respectively¹ [57], Eq. (3.18) can be recast as

$$\left[\sqrt{|g_{tt}|g_{rr}^{-1}} \left(r\sqrt{|g_{tt}|} \mathcal{F} \right)_{,r} \right]_{,r} + \omega^2 r\sqrt{g_{rr}} \mathcal{F} - |g_{tt}|\sqrt{g_{rr}} r^{-1} l(l+1) \mathcal{F} = 0. \quad (3.19)$$

Finally, using $\psi_e \equiv r\sqrt{|g_{tt}|} \mathcal{F}$ and introducing the tortoise coordinate, the perturbation equation is written as a Schrödinger-like equation as follows

$$\partial_{r_*}^2 \psi_e + \omega^2 \psi_e = V_e(r) \psi_e, \quad (3.20)$$

with the potential defined as

$$V_e(r) = |g_{tt}| \frac{l(l+1)}{r^2}. \quad (3.21)$$

The effect of l and η on the EM potential has been visualized in Fig. 6.

¹Here, $Y(\theta)$ is the Gegenbauer function [58].

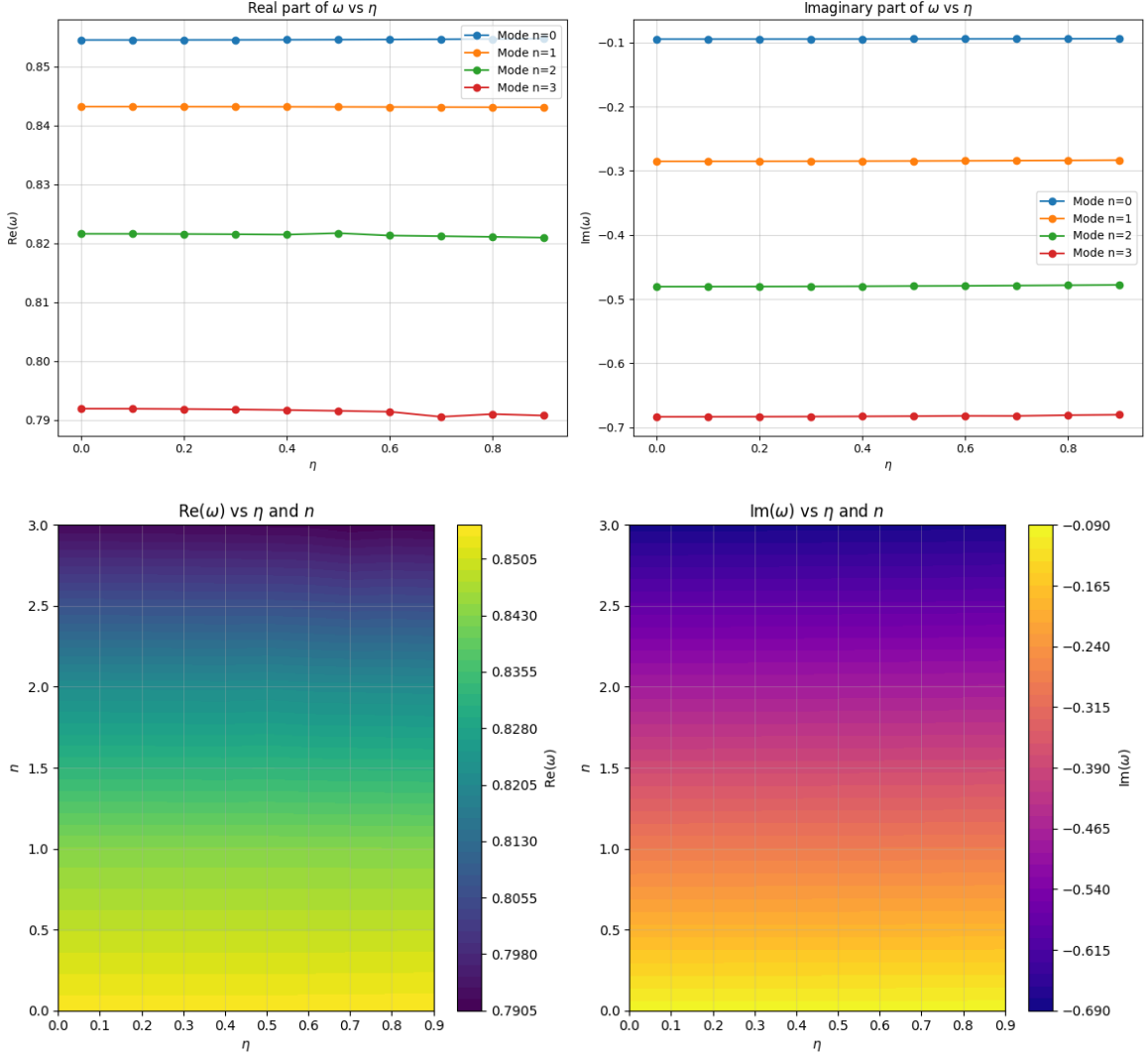


Figure 4: Variation of the $l = 4$ scalar QNMs with η and fixed $\ell = -0.01$.

3.3.1 Variation of EM QNMs with ℓ

The variation of the EM QNMs with ℓ is shown in the data listed in Table 3 and visualized in Fig. 7. As shown in the figure, as ℓ increases from -0.01 to 0 , ω_{Re} exhibits increasing behavior across all overtones. For instance, the fundamental mode increases from $\omega_{\text{Re}} \approx 0.840533$ at $\ell = -0.01$ to $\omega_{\text{Re}} \approx 0.853095$ at $\ell = 0$. This indicates that EM perturbations of the KR BH are weakly sensitive to ℓ . Next, ω_{Im} becomes more negative as ℓ increases, though the changes are subtle. For the fundamental mode, ω_{Im} changes from approximately -0.0939104 at $\ell = -0.01$ to -0.0958599 at $\ell = 0$. A similar trend is observed for the higher overtones. This indicates that the damping of the EM QNMs becomes slightly more efficient as ℓ increases. Physically, this may reflect a modification of the effective potential barrier, leading to enhanced leakage of energy from the perturbation field. As shown in Fig. 8, for the lower overtones ($n = 0$ and $n = 1$), the errors remain significantly small (on the order of 10^{-9} and 10^{-7} , respectively), suggesting robust numerical convergence of the WKB method

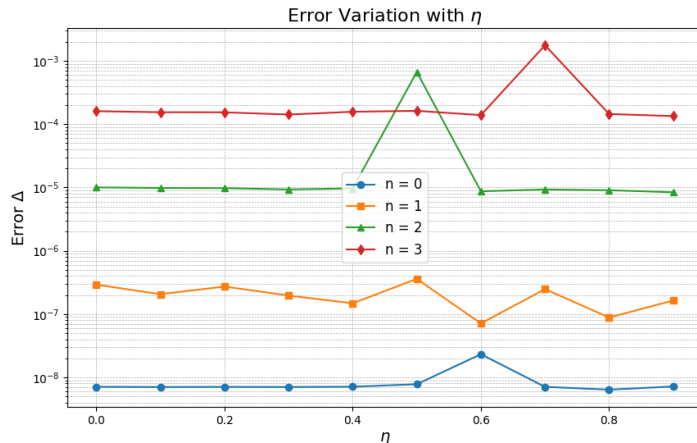


Figure 5: Errors in Table 2

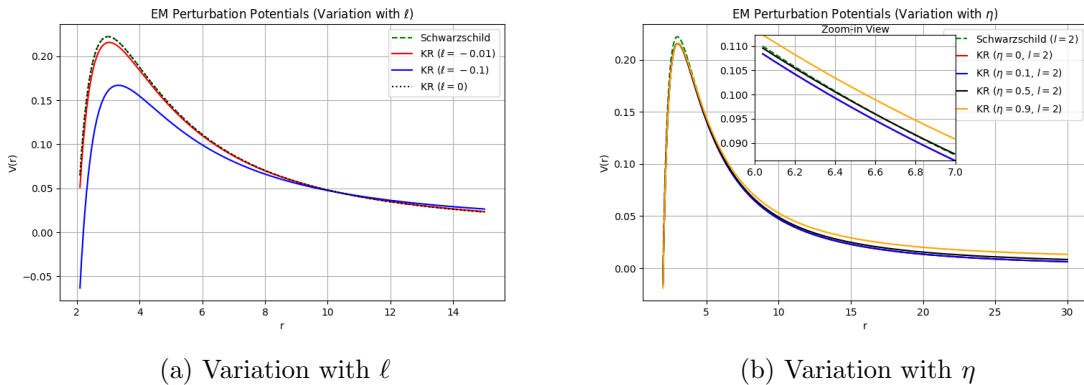


Figure 6: Variation of the EM potential with ℓ and η .

used. However, for the higher overtones ($n = 2$ and $n = 3$), certain values of ℓ exhibit larger errors. Notably, for $n = 2$ the error at $\ell = -0.002$ is an outlier, and a similar anomaly is observed for $n = 3$ at $\ell = -0.004$. These deviations could indicate increased sensitivity of the numerical method in the parameter space or potentially signal more intricate physical behavior in the effective potential near these parameter values.

3.3.2 Variation of EM QNMs with η

Here, we examine the variation of the EM QNM frequencies of the KR black hole as a function of the model parameter η , while keeping the multipole parameter fixed at $\ell = -0.01$. The real part of the EM QNM frequencies, ω_{Re} , exhibits systematic variation with η . For the fundamental mode, ω_{Re} remains nearly constant, with a value of approximately 0.84053. The higher overtones ($n = 1, 2, 3$) also exhibit subtle variations in ω_{Re} as η increases from 0 to 0.9. These trends suggest that EM perturbations are weakly sensitive to the parameter η when ℓ is fixed. Thus, the oscillation frequencies can be considered robust against variations in η . In contrast to the real part, ω_{Im} exhibits pronounced variations with η . For $n = 0$, ω_{Im} changes slightly from -0.09397 at $\eta = 0$ to approximately -0.09340 at $\eta = 0.9$, indicating a

ℓ	n	ω	Δ
-0.01	0	0.840533 - 0.0939104 <i>i</i>	8.05845×10^{-9}
	1	0.828964 - 0.283425 <i>i</i>	1.95094×10^{-7}
	2	0.806921 - 0.477888 <i>i</i>	0.000010659
	3	0.77663 - 0.680049 <i>i</i>	0.000171779
-0.008	0	0.84302 - 0.0942957 <i>i</i>	8.23541×10^{-9}
	1	0.831401 - 0.284589 <i>i</i>	2.76522×10^{-7}
	2	0.809259 - 0.479854 <i>i</i>	0.0000108714
	3	0.778834 - 0.682856 <i>i</i>	0.000174666
-0.006	0	0.84552 - 0.0946833 <i>i</i>	8.53950×10^{-9}
	1	0.833849 - 0.28576 <i>i</i>	3.03650×10^{-7}
	2	0.811609 - 0.481832 <i>i</i>	0.0000111374
	3	0.781051 - 0.68568 <i>i</i>	0.000179202
-0.004	0	0.848033 - 0.0950732 <i>i</i>	8.31609×10^{-9}
	1	0.836309 - 0.286938 <i>i</i>	2.14644×10^{-7}
	2	0.813971 - 0.483824 <i>i</i>	0.0000111912
	3	0.783283 - 0.688529 <i>i</i>	0.000177966
-0.002	0	0.850558 - 0.0954654 <i>i</i>	8.57299×10^{-9}
	1	0.838782 - 0.288123 <i>i</i>	3.04502×10^{-7}
	2	0.816688 - 0.485716 <i>i</i>	0.000729912
	3	0.785518 - 0.691381 <i>i</i>	0.000181332
0	0	0.853095 - 0.0958599 <i>i</i>	8.48987×10^{-9}
	1	0.841267 - 0.289315 <i>i</i>	2.44188×10^{-7}
	2	0.818728 - 0.48784 <i>i</i>	0.0000113506
	3	0.787769 - 0.694263 <i>i</i>	0.000180529

Table 3: Variation of $l = 4$ EM QNMs with ℓ and fixed $\eta = 0.3$

minor reduction in the damping rate. Similar behavior is observed for the higher overtones. Notably, although the absolute variations are small, the consistent decreasing trend of $|\omega_{\text{Im}}|$ with increasing η suggests that the damping of the EM QNMs is marginally reduced at higher values of the model parameter, which may be interpreted as a weakening of the dissipative mechanism, possibly due to subtle alterations in the effective potential's barrier height or width, which governs the leakage of energy from the perturbation. The errors in the fundamental mode ($n = 0$) are significantly small, indicating the high accuracy of the WKB method used. Similarly, the error estimates for the $n = 1$ mode remain on the order of 10^{-7} , except for minor fluctuations. For the higher overtones ($n = 2$ and $n = 3$), the errors are slightly larger and exhibit variability. For instance, for the error corresponding to $n = 2$ is on the order of 10^{-5} to 10^{-4} , while for $n = 3$ it ranges approximately between 10^{-4} and 10^{-3} . Some outliers are also noted (for example, at $\eta = 0.5$ for $n = 2$ or at $\eta = 0.6$ for $n = 3$). These anomalies might indicate either increased numerical sensitivity in the computation of higher overtones or possibly the emergence of resonant behavior.

3.4 Gravitational Perturbations

To evaluate axial gravitational perturbations in effective theories such as the one in our framework, it can be considered that the black hole is described by Einstein gravity minimally coupled to an anisotropic source, and perturbations can be considered as encoded in the

η	n	ω	Δ
0	0	$0.840531 - 0.0939748i$	8.42754×10^{-8}
	1	$0.828992 - 0.283609i$	8.80875×10^{-7}
	2	$0.806999 - 0.47817i$	0.0000135377
	3	$0.776772 - 0.680406i$	0.000175467
0.1	0	$0.840531 - 0.0939675i$	8.27932×10^{-9}
	1	$0.828989 - 0.283588i$	2.86915×10^{-7}
	2	$0.806968 - 0.478154i$	0.000047848
	3	$0.776717 - 0.680383i$	0.000133298
0.2	0	$0.840531 - 0.0939461i$	8.21734×10^{-9}
	1	$0.828979 - 0.283527i$	2.81217×10^{-7}
	2	$0.806961 - 0.478041i$	0.000010762
	3	$0.776692 - 0.680243i$	0.000169717
0.3	0	$0.840533 - 0.0939104i$	8.05845×10^{-9}
	1	$0.828964 - 0.283425i$	1.95094×10^{-7}
	2	$0.806921 - 0.477888i$	0.000010659
	3	$0.776663 - 0.680049i$	0.000171779
0.4	0	$0.840535 - 0.0938604i$	7.81494×10^{-9}
	1	$0.828944 - 0.283283i$	1.53101×10^{-7}
	2	$0.806864 - 0.477673i$	0.0000102767
	3	$0.776538 - 0.67979i$	0.000160844
0.5	0	$0.840539 - 0.0937962i$	6.91838×10^{-9}
	1	$0.828918 - 0.283101i$	4.79139×10^{-7}
	2	$0.806761 - 0.477425i$	0.0000876684
	3	$0.776197 - 0.679699i$	0.000228446
0.6	0	$0.840545 - 0.0937176i$	8.08020×10^{-9}
	1	$0.828888 - 0.282877i$	2.54925×10^{-7}
	2	$0.806704 - 0.477058i$	0.0000105373
	3	$0.78497 - 0.680625i$	0.0177751
0.7	0	$0.840555 - 0.0936248i$	8.29196×10^{-9}
	1	$0.828854 - 0.282613i$	2.94306×10^{-7}
	2	$0.806841 - 0.476598i$	0.000498975
	3	$0.776106 - 0.678519i$	0.000171347
0.8	0	$0.840569 - 0.0935177i$	8.11456×10^{-9}
	1	$0.828817 - 0.282309i$	2.65578×10^{-7}
	2	$0.806686 - 0.476132i$	0.000427405
	3	$0.775912 - 0.677949i$	0.000176698
0.9	0	$0.840589 - 0.0933962i$	1.45159×10^{-7}
	1	$0.828778 - 0.281963i$	2.54807×10^{-6}
	2	$0.806333 - 0.475672i$	0.0000144084
	3	$0.77553 - 0.677351i$	0.000102768

Table 4: Variation of $l = 4$ EM QNMs with η and fixed $\ell = -0.01$

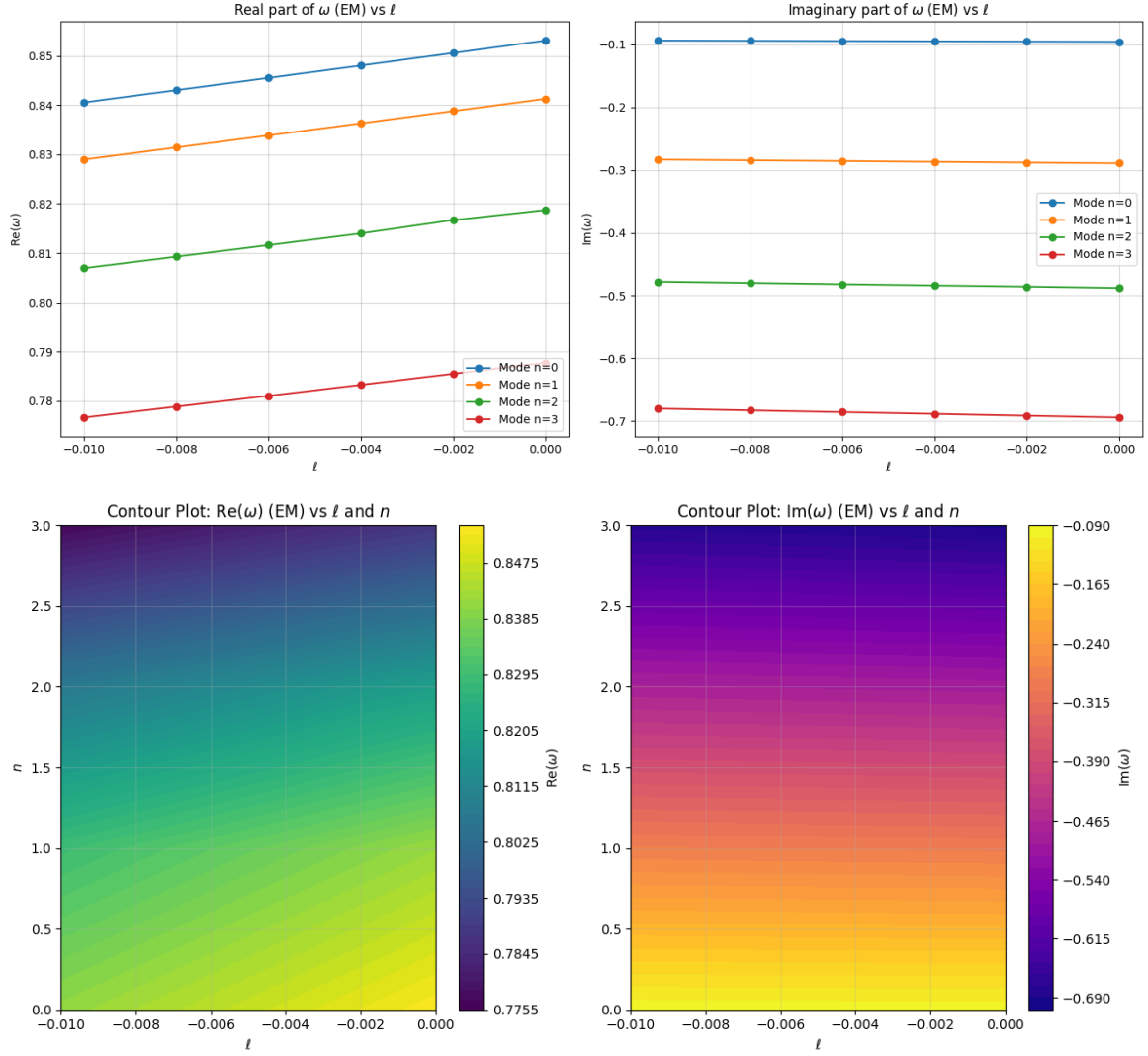


Figure 7: Variation of the $l = 4$ EM QNMs with l and fixed $\eta = 0.3$.

perturbations of the gravitational field equation and the corresponding anisotropic energy–momentum tensor. In the tetrad formalism, the axial components of perturbed energy–momentum tensor are zero [59], and thus, the master equation can be derived from $R_{(a)(b)} = 0$; the $\theta\phi$ and $r\phi$ components yield [56]

$$\left[r^2 \sqrt{|g_{tt}|g_{rr}^{-1}} (b_{,\theta} - c_{,r}) \right]_{,r} = r^2 \sqrt{|g_{tt}|^{-1}g_{rr}} (a_{,\theta} - c_{,t})_{,t}, \quad (3.22)$$

$$\left[r^2 \sqrt{|g_{tt}|g_{rr}^{-1}} (c_{,r} - b_{,\theta}) \sin^3 \theta \right]_{,\theta} = \frac{r^4 \sin^3 \theta}{\sqrt{|g_{tt}|g_{rr}}} (a_{,r} - b_{,t})_{,t}. \quad (3.23)$$

Now, considering the ansatz $\mathcal{F}_g(r, \theta) = \mathcal{F}_g(r)Y(\theta)$, using the redefinition $\psi_g r = \mathcal{F}_g$, and introducing the tortoise coordinate defined earlier, the master perturbation equation can be derived from Eqs. (3.22) and (3.23) as

$$\partial_{r_*}^2 \psi_g + \omega^2 \psi_g = V_g(r) \psi_g, \quad (3.24)$$

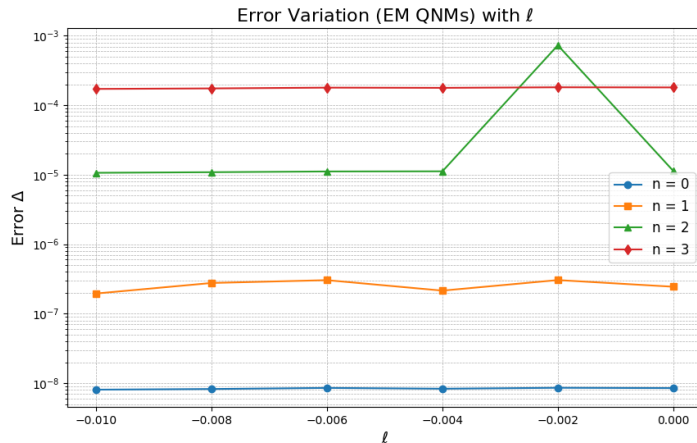


Figure 8: Errors in Table 3

where the effective potential is given by

$$V_g(r) = |g_{tt}| \left[\frac{2}{r^2} \left(\frac{1}{g_{rr}} - 1 \right) + \frac{l(l+1)}{r^2} - \frac{1}{r\sqrt{|g_{tt}|g_{rr}}} \left(\frac{d}{dr} \sqrt{|g_{tt}|g_{rr}^{-1}} \right) \right]. \quad (3.25)$$

The dependence of the gravitational perturbation potential on the model parameters l and η is shown in Fig. 11

3.4.1 Variation of gravitational QNMs with l

This section investigates the variation of the gravitational QNMs of the KR black hole with respect to the parameter l , while keeping the model parameter fixed at $\eta = 0.3$. The estimated frequency-domain data are presented in Table 5 and visualized in Fig. 12. It can be seen that ω_{Re} exhibits an increasing trend with l for all overtones. For instance, in the fundamental mode ($n = 0$), ω_{Re} increases from approximately 0.8260 at $l = -0.01$ to 0.8386 at $l = 0$. This trend is consistent across higher overtones. The physical interpretation of this trend lies in the nature of the effective potential governing gravitational perturbations. Moreover, ω_{Im} , which determines the damping rate, also exhibits a systematic variation with l . Specifically, a steady increase in the magnitude of ω_{Im} (that is, it becomes more negative) is observed with increasing l . For the fundamental mode, ω_{Im} changes from approximately -0.09336 at $l = -0.01$ to -0.09531 at $l = 0$. The trend is more pronounced for higher overtones. This behavior suggests that perturbations decay more rapidly for larger values of l , implying enhanced damping. The relative errors Δ corresponding to the estimated QNMs are generally small, indicating good numerical convergence. For the fundamental mode, the errors remain on the order of 10^{-8} to 10^{-9} . For $n = 1$, the errors are slightly larger (on the order of 10^{-7}), but within acceptable limits. For the higher overtones ($n = 2, 3$), the errors show higher variability. Notably, for $n = 2$, the error at $l = -0.01$ is significantly larger (~ 0.00085), while for other l values, it remains on the order of 10^{-5} to 10^{-6} . This suggests that numerical accuracy is sensitive for higher overtones.

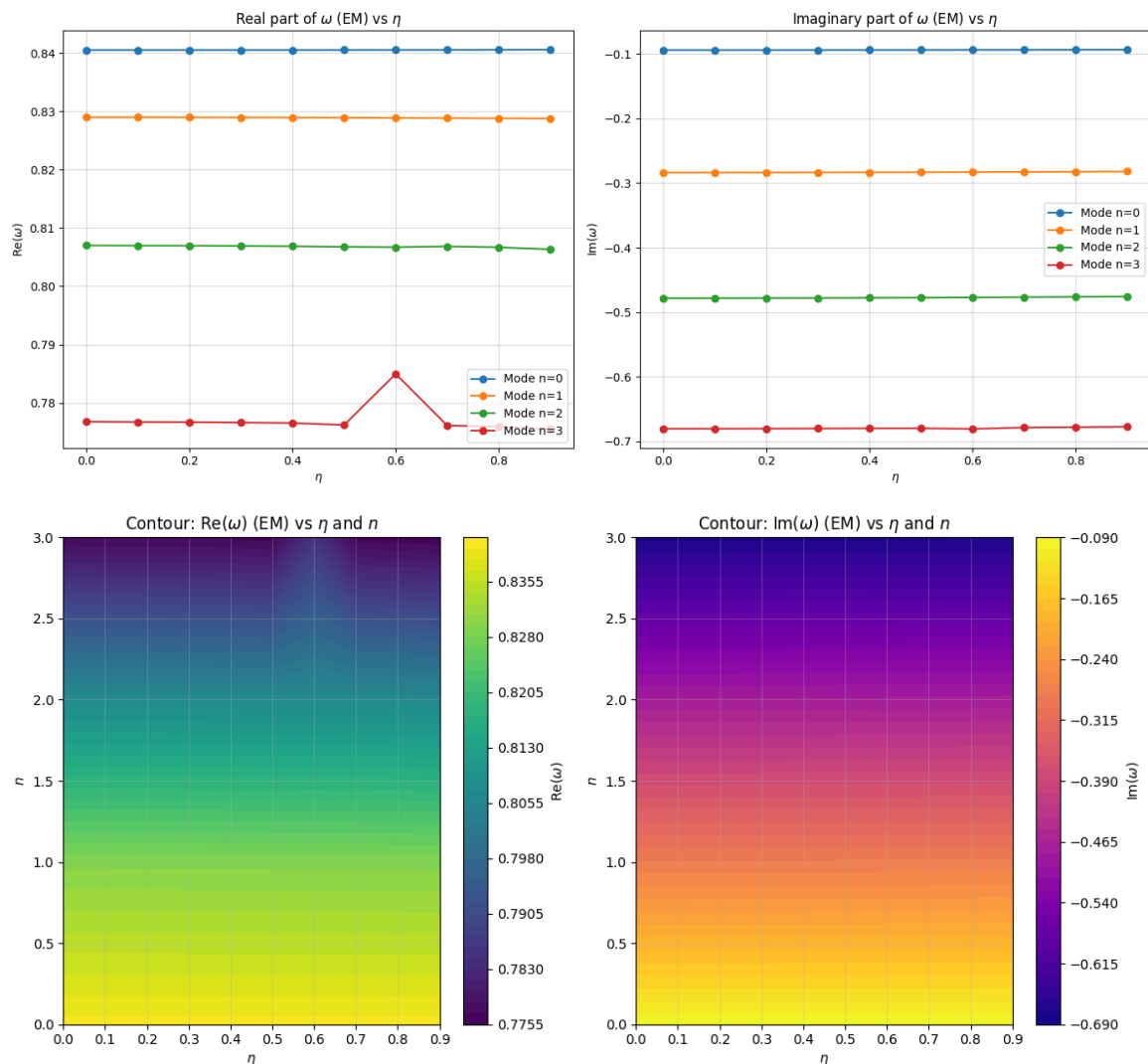


Figure 9: Variation of the $l = 4$ EM QNMs with η and fixed $\ell = -0.01$.

3.4.2 Variation of gravitational QNMs with η

The estimated QNM frequencies for gravitational perturbations of the KR black hole are presented in Table 6 and visualized in Fig. 14. It can be seen that ω_{Re} exhibits subtle increases with η for all overtones. For the fundamental mode, ω_{Re} increases slightly from 0.82598 at $\eta = 0$ to 0.82638 at $\eta = 0.9$. This increasing trend is consistently observed for higher overtones. The weak dependence of ω_{Re} on η suggests that the oscillatory behavior of the gravitational perturbations is largely insensitive to variations in this model parameter. In contrast, ω_{Im} exhibits a stronger dependence on η . The magnitude of ω_{Im} (damping rate) decreases as η increases. For $n = 0$, ω_{Im} increases from -0.09344 at $\eta = 0$ to -0.09270 at $\eta = 0.9$. This trend is consistent for the higher overtones, suggesting that perturbations decay more slowly (are long lived) as η increases. A critical aspect of our analysis is the evaluation of the numerical errors associated with the estimated QNMs. For the fundamental mode, the errors remain significantly small ($\sim 10^{-8}$), indicating high precision. For $n = 1$,

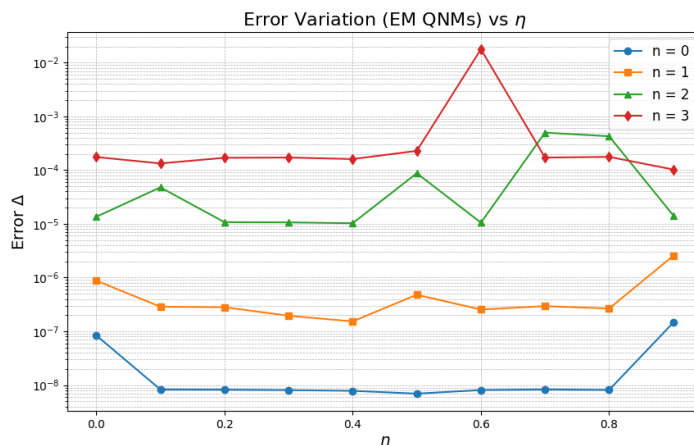


Figure 10: Errors in Table 4

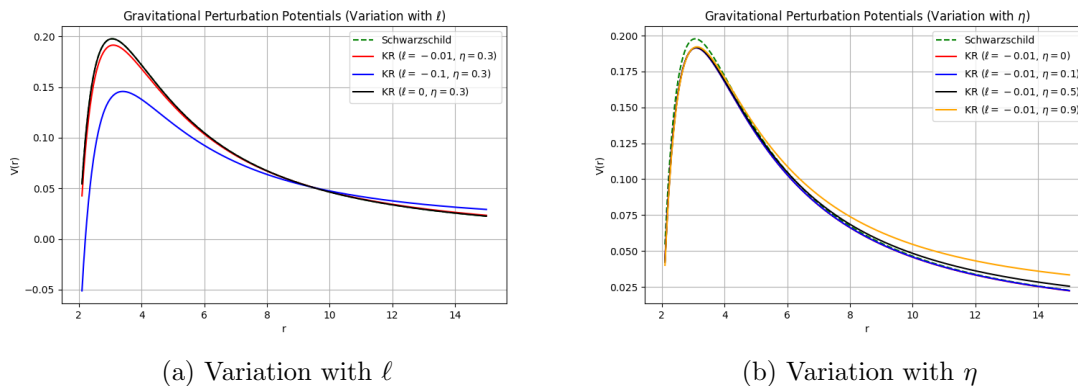


Figure 11: Variation of the gravitational perturbation potential with ℓ and η .

the errors are slightly larger ($\sim 10^{-7}$), but remain well-controlled. The higher overtones ($n = 2, 3$) exhibit larger errors, especially at certain values of η . Notably, for $n = 2$, the error peaks at $\eta = 0.3$ with $\Delta \sim 0.00085$, while for $n = 3$, fluctuations occur at multiple points, particularly near $\eta = 0.5$. These anomalies may be attributed to numerical sensitivity of higher overtones. However, the overall error estimates remain within reasonable limits, supporting the reliability of the Pade-averaged WKB method.

3.5 Time-domain QNMs

The wave-like equation for perturbations can be written *without* implying a stationary ansatz as [54]:

$$\frac{\partial^2 \Phi}{\partial t^2} - \frac{\partial^2 \Phi}{\partial x^2} + V(t, x) \Phi = 0, \quad (3.26)$$

Here, we denote the tortoise coordinate by x . The most widely discussed method to integrate the above wave equation in the time domain was developed by Gundlach, Price and Pullin

ℓ	n	ω	Δ
-0.01	0	0.826017 - 0.0933595 <i>i</i>	1.60512×10^{-8}
	1	0.814202 - 0.281814 <i>i</i>	3.56186×10^{-7}
	2	0.792106 - 0.475256 <i>i</i>	0.000852838
	3	0.760776 - 0.676758 <i>i</i>	0.000192527
-0.008	0	0.828511 - 0.0937451 <i>i</i>	9.86473×10^{-9}
	1	0.816648 - 0.282978 <i>i</i>	1.850345×10^{-7}
	2	0.794047 - 0.477304 <i>i</i>	0.0000119645
	3	0.763007 - 0.679562 <i>i</i>	0.000190059
-0.006	0	0.831017 - 0.094133 <i>i</i>	1.08987×10^{-8}
	1	0.819107 - 0.284148 <i>i</i>	3.16565×10^{-7}
	2	0.796411 - 0.479276 <i>i</i>	0.0000118237
	3	0.765234 - 0.68236 <i>i</i>	0.00018886
-0.004	0	0.833537 - 0.0945231 <i>i</i>	9.92957×10^{-9}
	1	0.821578 - 0.285326 <i>i</i>	1.64192×10^{-7}
	2	0.79879 - 0.481264 <i>i</i>	0.0000121857
	3	0.767494 - 0.685205 <i>i</i>	0.000192962
-0.002	0	0.836069 - 0.0949156 <i>i</i>	2.03060×10^{-8}
	1	0.824061 - 0.286509 <i>i</i>	5.48275×10^{-7}
	2	0.801176 - 0.483257 <i>i</i>	0.0000132747
	3	0.769734 - 0.688039 <i>i</i>	0.000205674
0	0	0.838615 - 0.0953104 <i>i</i>	1.10228×10^{-8}
	1	0.826557 - 0.287701 <i>i</i>	2.51917×10^{-7}
	2	0.80358 - 0.485269 <i>i</i>	0.0000123588
	3	0.772017 - 0.690916 <i>i</i>	0.000192333

Table 5: Variation of $l = 4$ gravitational QNMs with ℓ and fixed $\eta = 0.3$

[60, 61]; we call this the GPP method. In terms of *light-cone coordinates* $du = dt - dx$ and $dv = dt + dx$, the above equation can be rewritten as:

$$\left(4 \frac{\partial^2}{\partial u \partial v} + V(u, v)\right) \Phi(u, v) = 0. \quad (3.27)$$

The following discretization scheme is as per the GPP method:

$$\Phi(N) = \Phi(W) + \Phi(E) - \Phi(S) - \frac{h^2}{8} V(S) (\Phi(W) + \Phi(E)) + \mathcal{O}(h^4), \quad (3.28)$$

where we introduced letters to mark the points as follows: $S = (u, v)$, $W = (u + h, v)$, $E = (u, v + h)$, and $N = (u + h, v + h)$.

In this *double-null* scheme, we specify appropriate initial data (Gaussian in this case) and find the time-domain profile data $\{\Phi(t = t_0), \Phi(t = t_0 + h), \Phi(t = t_0 + 2h), \dots\}$. We start by visualizing the time-domain profile for scalar perturbations for the $l = 2$ mode with $\ell = -0.01$ and $\eta = 0.3$. An initial Gaussian pulse centered at $v_c = 20$ with width $\sigma = 2.5$ is used. In the numerical scheme, we appropriately handle the coordinate transformation ($r \rightarrow r_*$ and vice versa) and extract the signal at $r = 8$ ($r_* \sim 14.75$) for reference. The resulting time-domain profile is shown in Fig. 16a. Similarly, using the effective potentials

η	n	ω	Δ
0	0	$0.825977 - 0.0934407i$	7.98485×10^{-8}
	1	$0.81421 - 0.282043i$	1.77510×10^{-6}
	2	$0.79179 - 0.475685i$	0.0000273425
	3	$0.761013 - 0.677201i$	0.000235264
0.1	0	$0.825981 - 0.0934315i$	9.83194×10^{-9}
	1	$0.81421 - 0.282016i$	1.97713×10^{-7}
	2	$0.791769 - 0.475636i$	0.0000118918
	3	$0.760921 - 0.677105i$	0.000194114
0.2	0	$0.825994 - 0.0934046i$	7.02244×10^{-9}
	1	$0.814207 - 0.281941i$	1.28577×10^{-7}
	2	$0.791742 - 0.475527i$	0.0000121541
	3	$0.760877 - 0.676987i$	0.00018912
0.3	0	$0.826017 - 0.0933595i$	1.60512×10^{-8}
	1	$0.814202 - 0.281814i$	3.56186×10^{-7}
	2	$0.792106 - 0.475256i$	0.000852838
	3	$0.760776 - 0.676758i$	0.000192527
0.4	0	$0.826049 - 0.0932963i$	9.70264×10^{-9}
	1	$0.814196 - 0.281638i$	1.77838×10^{-7}
	2	$0.791628 - 0.475085i$	0.0000117009
	3	$0.760658 - 0.67647i$	0.000180624
0.5	0	$0.826091 - 0.0932151i$	2.47987×10^{-8}
	1	$0.814188 - 0.281413i$	7.26756×10^{-7}
	2	$0.791552 - 0.474761i$	0.0000172737
	3	$0.760553 - 0.67609i$	0.000210213
0.6	0	$0.826144 - 0.0931154i$	1.10924×10^{-8}
	1	$0.814181 - 0.281134i$	2.68198×10^{-7}
	2	$0.791441 - 0.474351i$	0.0000113473
	3	$0.760305 - 0.675597i$	0.000181959
0.7	0	$0.82621 - 0.0929975i$	1.02441×10^{-8}
	1	$0.814173 - 0.280806i$	2.01366×10^{-7}
	2	$0.791322 - 0.473876i$	0.0000107261
	3	$0.760081 - 0.675046i$	0.000169263
0.8	0	$0.826289 - 0.0928612i$	9.58757×10^{-9}
	1	$0.814167 - 0.280428i$	1.09999×10^{-7}
	2	$0.791187 - 0.473329i$	0.0000109236
	3	$0.759823 - 0.674407i$	0.000167509
0.9	0	$0.826383 - 0.0927061i$	1.03704×10^{-8}
	1	$0.814163 - 0.279998i$	1.40012×10^{-7}
	2	$0.791032 - 0.472708i$	9.98827×10^{-6}
	3	$0.759521 - 0.673683i$	0.000152942

Table 6: Variation of $l = 4$ gravitational QNMs with η and fixed $\ell = -0.01$

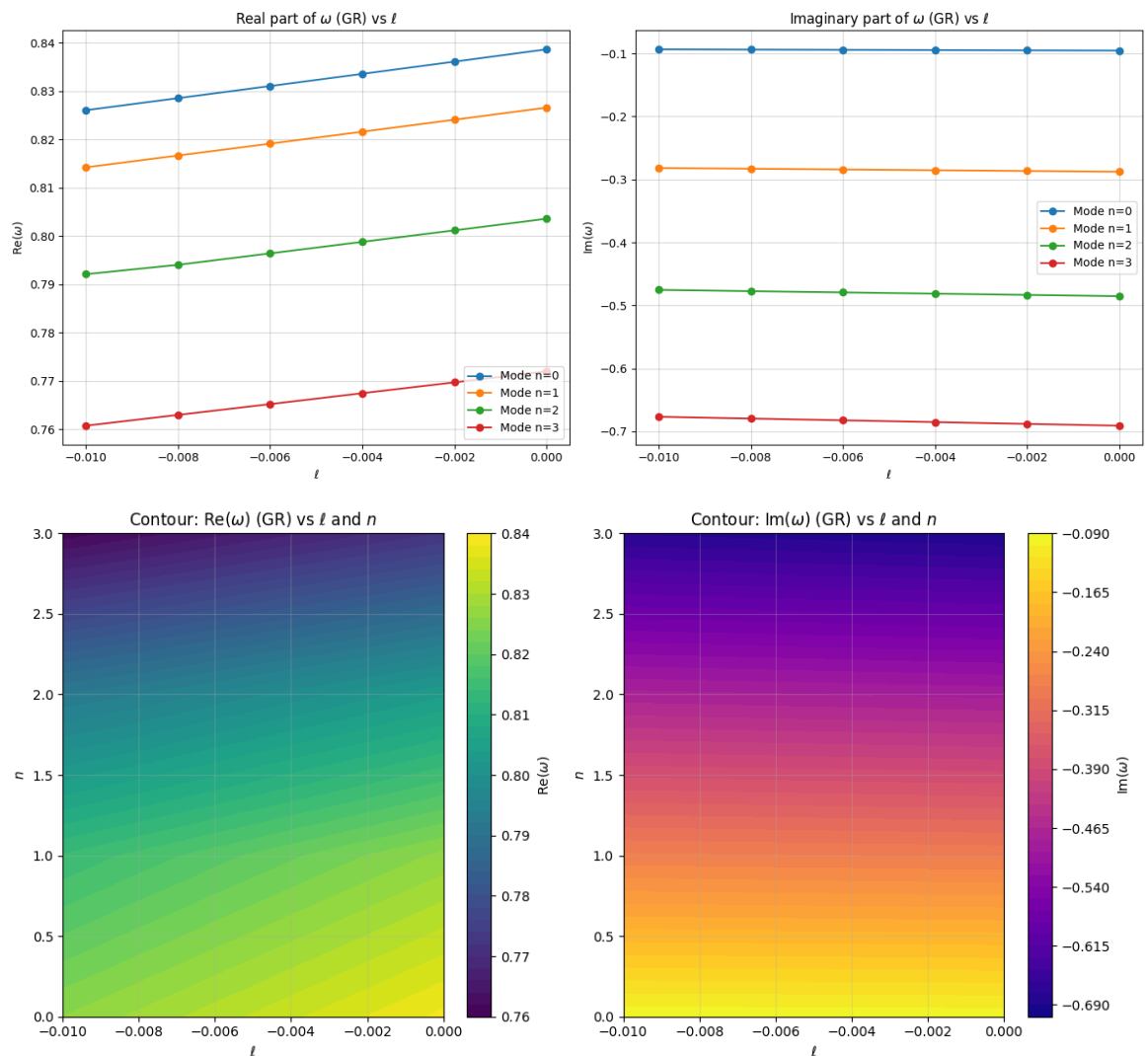


Figure 12: Variation of the $l = 4$ gravitational QNMs with l and fixed $\eta = 0.3$.

for EM and gravitational perturbations in the same parameter region, we evaluated the corresponding time-domain profiles using the GPP method, as shown in Figs. 17a and 18a. As discussed in the next section, we extract the corresponding QNMs from the time-domain signals with reasonable accuracy, and the behavior of the profiles with l and η are expected to retain the same dependence as that in the frequency-domain calculations.

3.6 Frequency extraction using the Prony method

For the ringdown (QNM-dominated) portion of the signal, the Prony method approximates the signal by a sum of exponentially damped sinusoids [62], one form of which can be written as:

$$\psi(t) = \sum_k A_k e^{-i\omega_k t}, \quad (3.29)$$

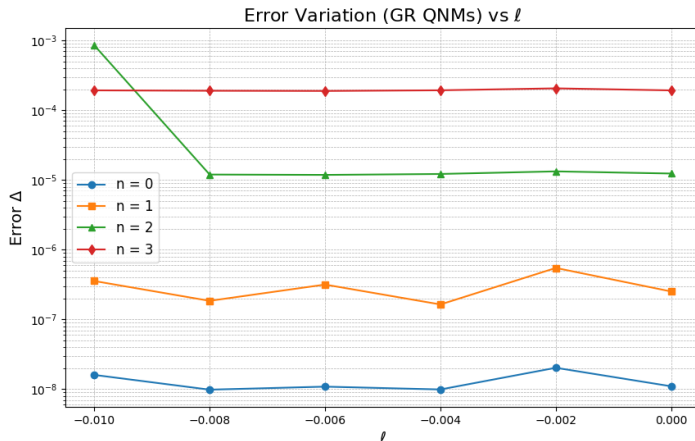


Figure 13: Errors in Table 5

with complex frequencies $\omega_k = \omega_{R,k} - i\gamma_k$ (where $\gamma_k > 0$ for damped modes). For a sampling time Δt in the discrete time domain, we have

$$z_k = \exp(-i\omega_k \Delta t). \quad (3.30)$$

The Prony method assumes a linear recurrence among the data and solves a linear least-squares problem to determine a polynomial whose roots z_k yield the QNM frequencies via

$$\omega_k = \frac{i}{\Delta t} \ln(z_k). \quad (3.31)$$

Then, physical modes can be identified by requiring $\omega_{R,k} > 0$ (oscillatory behavior) and $\gamma_k > 0$ (damping, corresponding to $\text{Im}(\omega_k) < 0$). Fig. 16b shows the fitting window of the time-domain profile for scalar perturbations and Fig. 16c shows the Prony fit to the time-domain signal. The estimated dominant QNM for the scalar case using the Prony method is $\omega_{0,2} = 0.487264 - 0.089473i$, and that estimated using the Padé-averaged WKB method is $\omega_{0,2} = 0.476361 - 0.0948474i$. Thus, the QNM frequency is extracted with reasonable accuracy. For the EM case, the Prony-extracted dominant QNM is $\omega_{0,2} = 0.461418 - 0.088815i$, and that using the Padé-averaged WKB method is $0.45096 - 0.0930865i$. For the gravitational case, the Prony-extracted frequency is $\omega_{0,2} = 0.433645 - 0.087799i$ and that extracted using the Padé-averaged WKB method is $\omega_{0,2} = 0.423823 - 0.0911131i$.

4 Greybody Factors and Sparsity of Hawking Radiation

4.1 Greybody Factors

In this section, we discuss the bounds on the GBFs. Drawing from the insights on the influence of the model parameters on the QNMs presented in the previous sections, we the GBFs associated with scalar perturbations and explore the impact of the model parameters on these bounds through an analytical approach. Analytical techniques for forecasting rigorous bounds on GBFs were first devised by Visser [63] and then improved by Boonserm *et al.* [64]. More detailed investigations of these bounds have been reported by Boonserm *et al.*, Yang *et*

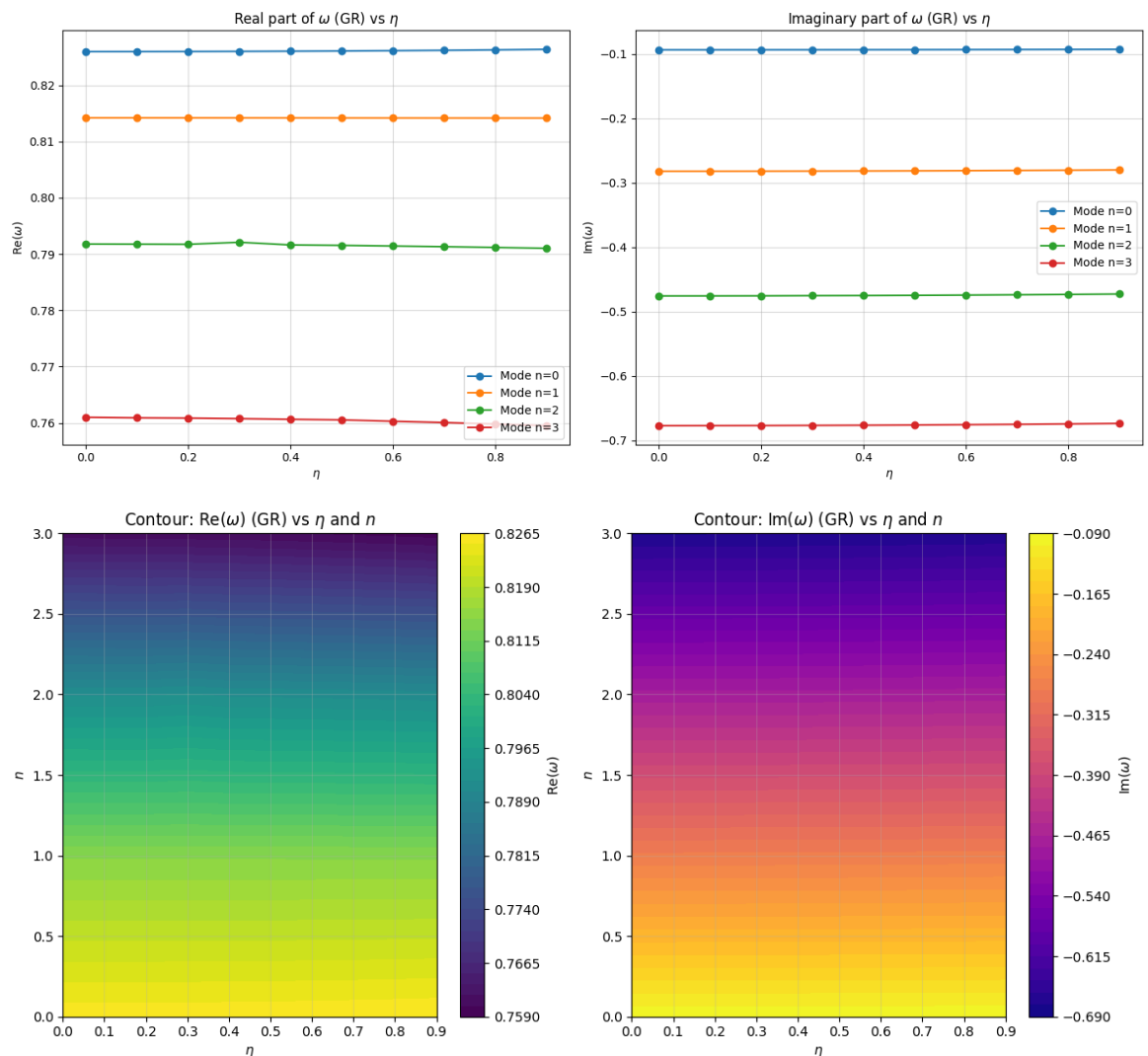


Figure 14: Variation of the $l = 4$ gravitational QNMs with η and fixed $\ell = -0.01$.

al. [65], Gray *et al.* [66], Ngampitipan *et al.* [67], and others [68–73]. In the present case, we extend this investigation by analyzing a BH solution influenced by a global monopole within a self-interacting KR field, thereby enhancing our insight into GBFs in a different context.

We consider the Klein-Gordon equation of the massless scalar field, as described in the previous section. The reduced effective potential, $V_{eff}(r)$, is given by:

$$V_{eff}(r) = \frac{l(l+1)A(r)}{r^2} + \frac{A(r)A'(r)}{r}. \quad (4.1)$$

We use the effective potential to investigate the lower bound of the GBFs in our BH solution. Following the work of Visser [63] and Boonserm [64], a suitable method for determining this strict bound is provided by

$$A_g^2 \geq \text{sech}^2 \left(\frac{1}{2\omega} \int_{-\infty}^{\infty} |V| \frac{dr}{A(r)} \right), \quad (4.2)$$

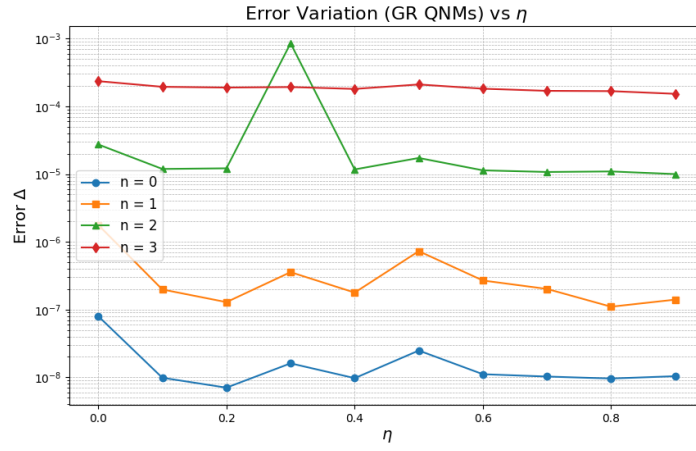
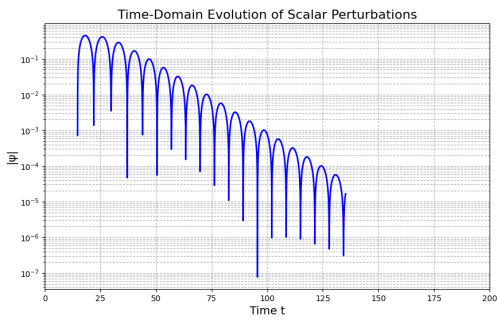
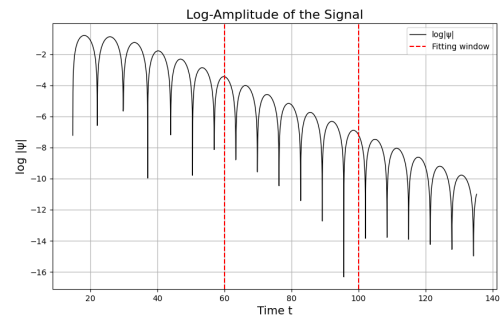


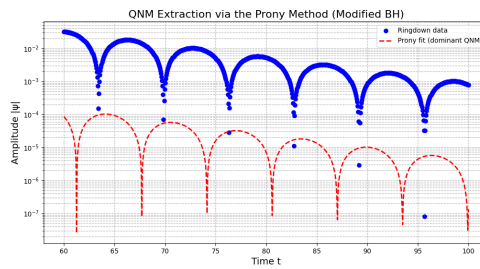
Figure 15: Errors in Table 6



(a) Time domain profile for scalar perturbations



(b) Log-amplitude and fitting window



(c) Prony fit of the time domain profile

Figure 16: Time domain profiles and Prony extraction for scalar perturbations

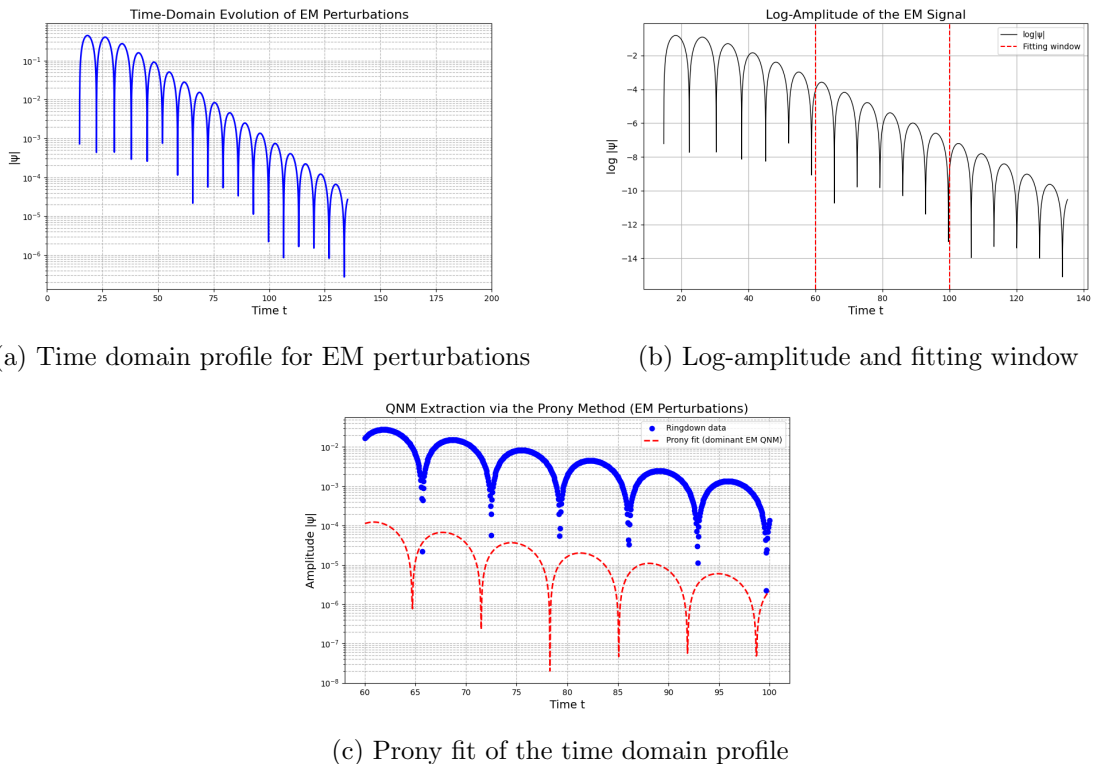


Figure 17: Time domain profiles and Prony extraction for EM perturbations

where A_g^2 denotes the transmission coefficient.

Moreover, to account for the cosmological horizon-like effect as a term of the metric function, we adjust the boundary conditions as described by Boonserm *et al.* [74]. The modified boundary condition is given by:

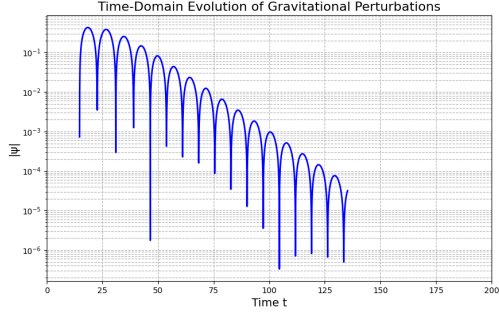
$$A_g^2 \geq A_s^2 = \text{sech}^2 \left(\frac{1}{2\omega} \int_{r_H}^{R_H} \frac{|V_{eff}|}{A(r)} dr \right) = \text{sech}^2 \left(\frac{A_l}{2\omega} \right), \quad (4.3)$$

where we define

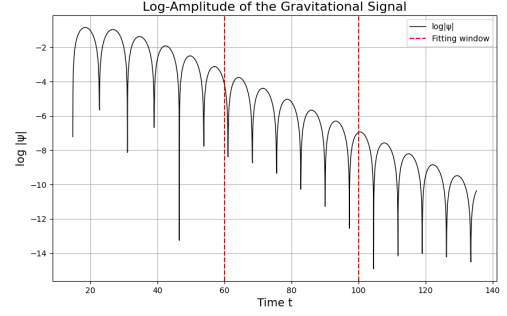
$$A_l = \int_{r_H}^{R_H} \frac{|V|}{A(r)} dr = \int_{r_H}^{R_H} \left| \frac{l(l+1)}{r^2} + \frac{A'(r)}{r} \right| dr. \quad (4.4)$$

Here, r_H is the event horizon and R_H is the cosmological horizon of the BH. This specification provides a rigorous lower bound on the GBFs corresponding to the BH solution.

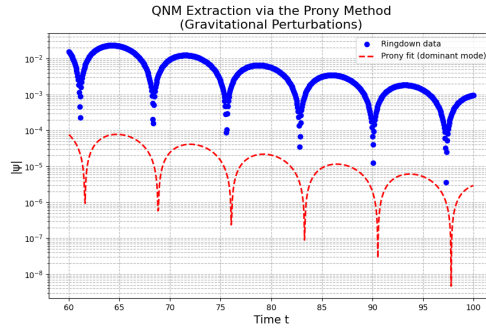
The behavior of the greybody bounds as a function of the model parameter is presented graphically in Figs. 19-21. In the range $\ell^- \cup \ell^+$, we investigate how a change of sign in ℓ affects the corresponding behavior of the GBFs. We also study the variation with the global monopole charge and multipole moment l . It can be seen that the variation of the greybody bound with respect to l for $\ell < 0$ or $\ell > 0$ remains unchanged (see Figs. 19a-19b). In turn, the variation of the KR parameter ℓ spanned out across $\ell^- \cup \ell^+$ presents a detailed behavior of the greybody bound (see Figs. 20a-20b). In this regime, the greybody boundary increases with decreasing ℓ in the ℓ^+ range (20a). By contrast, the increasing variation of the KR parameter ℓ in ℓ^- space leads to a decrease in the greybody bound (20b). Figs. 21a-21b highlight the effect of the global monopole charge η on the greybody bound. For



(a) Time domain profile for gravitational perturbations

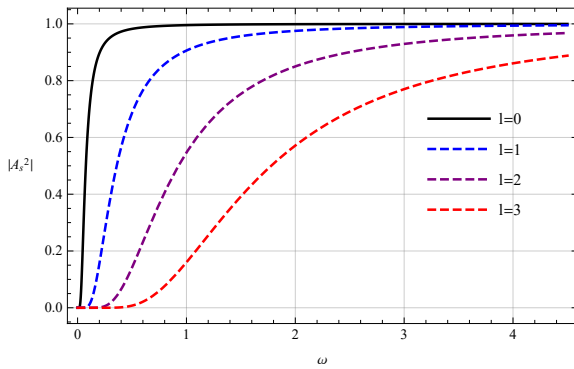


(b) Log-amplitude and fitting window

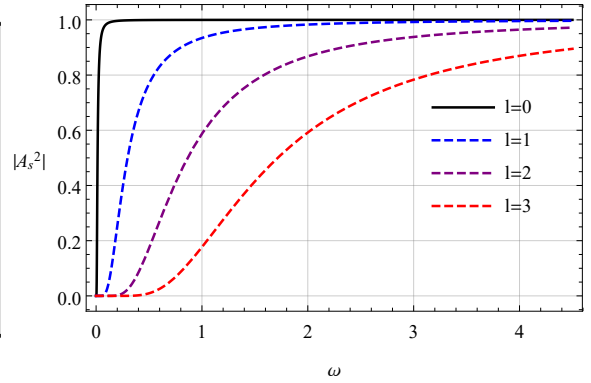


(c) Prony fit of the time domain profile

Figure 18: Time domain profiles and Prony extraction for EM perturbations



(a) Variation with l



(b) Variation with l

Figure 19: Rigorous bounds on greybody factors using $M = 1, \eta = 0.9$. On the left panel, $\ell = 0.1$ and on the right panel $\ell = -0.1$.

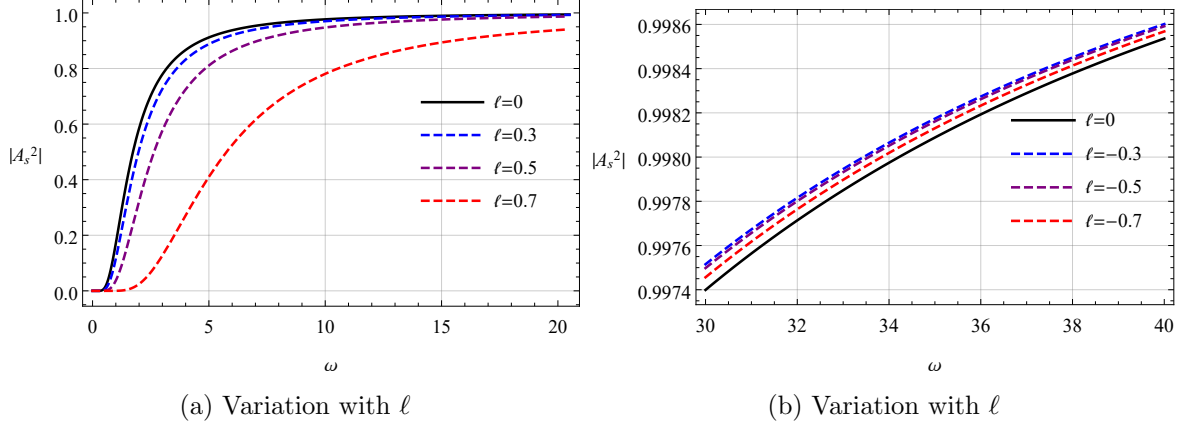


Figure 20: Rigorous bounds on greybody factors using $M = 1, \eta = 0.9$. On the left panel, $\ell \geq 0.1$ and on the right panel $\ell \leq -0.1$.

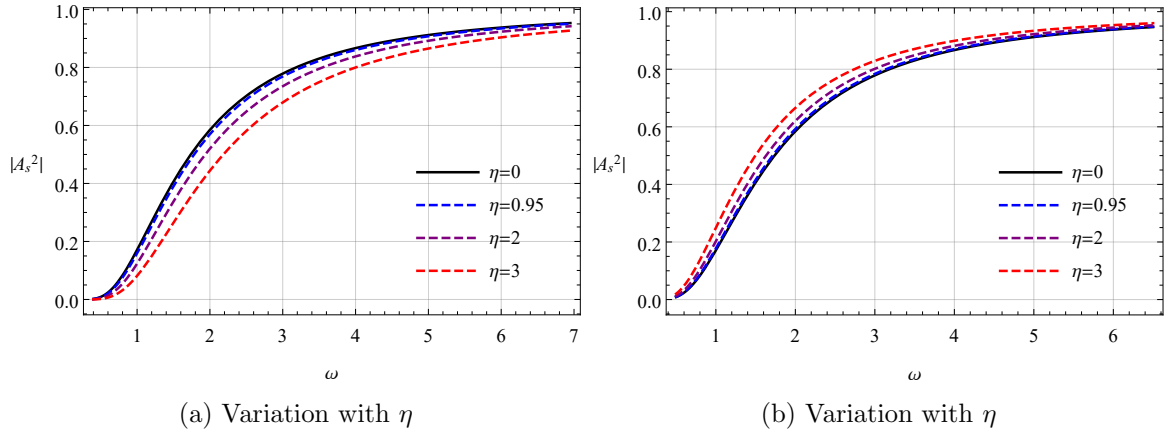


Figure 21: Rigorous bounds on greybody factors using $M = 1, l = 3$. On the left panel, $\ell = 0.1$ and on the right panel $\ell = -0.1$.

an increasing value of the KR field with $\ell = +0.1$ (Fig. 21a), the greybody bound tends to decrease, while for $\ell = -0.1$ (Fig. 21b), the grey body bound increases. Overall, the parameters η and ℓ affect the greybody behaviors in a non-trivial manner, as expected from the previous discussion of the scalar potential and corresponding QNMs.

4.2 Sparsity of Hawking Radiation

This section presents analyses on the sparsity Hawking radiation from the KR BH. Typically, a BH behaves analogously to a blackbody, emitting particles at a temperature close to the surface gravity. However, the Hawking radiation flux differs significantly from standard blackbody radiation in that it appears exceedingly sparse during the evaporation process. Sparsity is described as the mean time elapsed between the emission of consecutive quanta on time scales dictated by the energies of these quanta. It is defined as [75–78]

$$\tilde{\eta} = \frac{\mathcal{C}}{\tilde{g}} \left(\frac{\lambda_t^2}{\mathcal{A}_{eff}} \right), \quad (4.5)$$

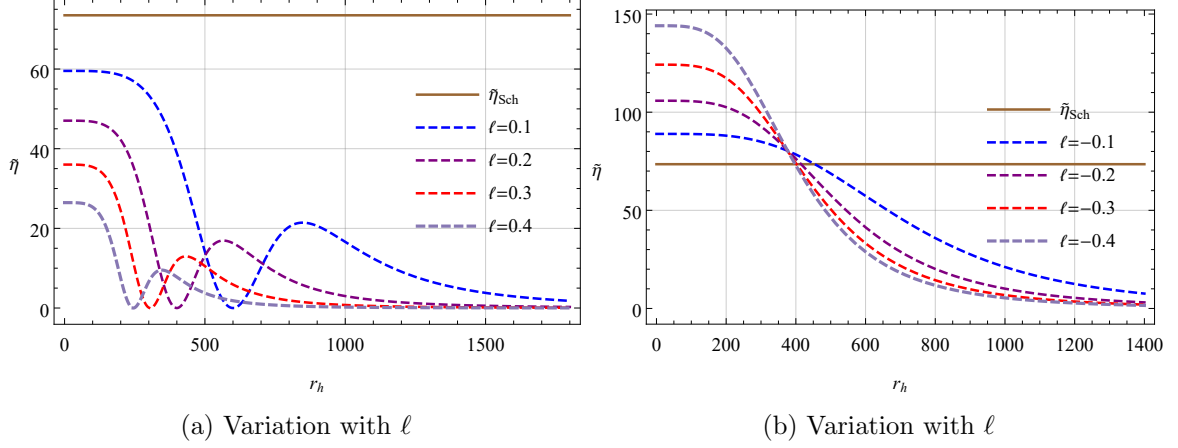


Figure 22: Sparsity of Hawking radiation against r_h using $\eta = 0.01$. On the left panel, $\ell \geq 0.1$ and on the right panel $\ell \leq -0.1$.

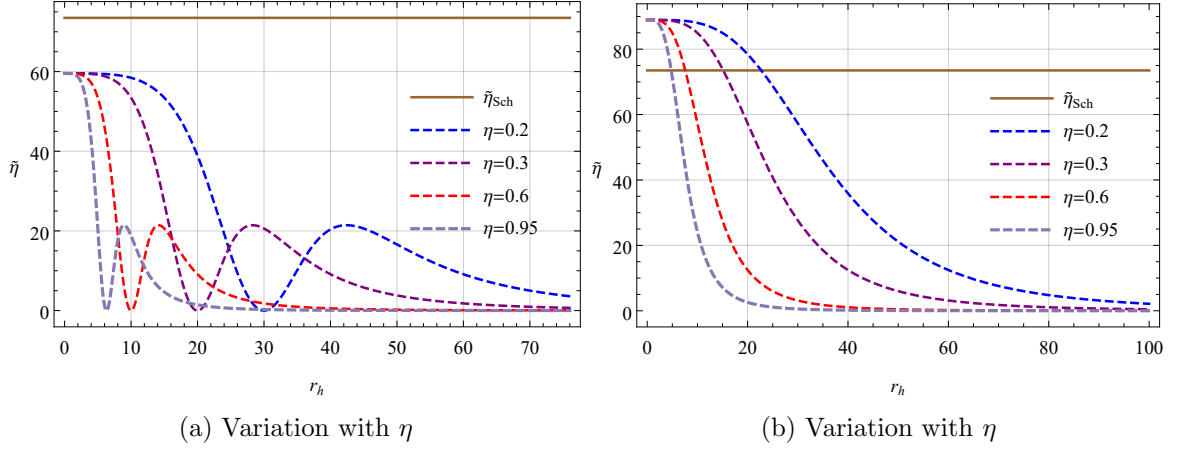


Figure 23: Sparsity of Hawking radiation against r_h . On the left panel, $\ell = 0.1$ and on the right panel $\ell = -0.1$.

where $\lambda_t = 2\pi/T$ denotes the thermal wavelength, $\mathcal{A}_{eff} = 27\mathcal{A}_{BH}/4$ acts as the effective surface area of the BH, \mathcal{C} is a dimensionless constant, and \tilde{g} represents the spin degeneracy factor of the emitted quanta. Thus, $\lambda_t = 8\pi r_h^2 \implies \eta_{Sch} = 64\pi^3/27 \approx 73.49$ is obtained for the simple case of a Schwarzschild BH and spin-1 bosons with no emitted mass. Note that $\eta \ll 1$ for black body radiation under comparison.

To analyze the sparsity behavior of Hawking radiation, it is useful to look at the corresponding Hawking temperature, which is defined as follows:

$$T = \frac{1}{4\pi} \left(\frac{dA(r)}{dr} \right)_{r=r_h} \quad (4.6)$$

from which the sparsity of Hawking radiation in terms of the parameter space can be expressed according to the following form:

$$\tilde{\eta} = \frac{256\pi^3(\ell - 1)^4 (\ell (\eta^2 r^2 + 4) - 4)^2}{3(\eta^4 \ell^2 r^4 + 6\eta^2(\ell - 1)\ell r^2 + 24(\ell - 1)^2)^2}. \quad (4.7)$$

It is expected that the model parameters would affect the behavior of the sparsity. Specifically, the choice of the partial set ($\ell = 0, \eta = 0$) allows us to probe a reduced form of the relevant sparsity such that

$$\tilde{\eta}(\ell = 0, \eta = 0) = \frac{64\pi^2}{27}, \quad (4.8)$$

in which the corresponding sparsity across this limit matches that of the Schwarzschild case exactly. In addition, a closer examination shows that the corresponding sparsity (4.7) coincides with the Schwarzschild one at

$$r_h^c = \sqrt{\frac{(\ell - 1) \left(\sqrt{3} \sqrt{\ell(3\ell - 8)} - 3\ell \right)}{\eta^2 \ell}} \quad (4.9)$$

where $\ell \leq -0.1$.

To unveil some of the scenarios characteristic of the study of sparsity in Hawking radiation, we need to examine the center the related behavior such that

$$\lim_{r_h \rightarrow 0} \tilde{\eta} \approx \frac{64}{27} \pi^3 (\ell - 1)^2, \quad (4.10)$$

where the KR parameter ℓ affects the sparsity behavior at the center, generating three possible scenarios; the first scenario implies that the corresponding sparsity is exactly that of the Schwarzschild spacetime when $\ell = 0$, the second scenario implies that $\tilde{\eta} < \tilde{\eta}_{Sch}$ when $\ell > 0$, and the third serves to present the desired observation $\tilde{\eta} > \tilde{\eta}_{Sch}$ when $\ell < 0$. By contrast, the large-distance sparsity of Hawking radiation provides

$$\lim_{r_h \rightarrow \infty} \tilde{\eta} \approx 0, \quad (4.11)$$

which indicates that $\tilde{\eta}$ decreases monotonically and asymptotically approaches zero.

To interpret the behavior of the corresponding sparsity graphically, Figs. 22-23 describe the appropriate variation of the sparsity $\tilde{\eta}$ as a function of the event horizon r_h . In this respect, two scenarios are proposed; specifically, $\ell < 0$ (Figs. 22b and 23b) and $\ell > 0$ (Figs. 22a and 23a). First, the scenario with $\ell > 0$ is significantly more similar for both variations of ℓ and η , which depicts that for sufficiently small r_h , the sparsity lies below the standard value η_{Sch} , indicating that the emitted radiation is less sparse (more sparse for $\ell < 0$) than the Hawking radiation at this evaporation stage. This is in contrast to the $\ell < 0$ scenario, entailing at small r_h , the relation $\tilde{\eta} > \tilde{\eta}_{Sch}$ (Figs. 22b and 23b). As the event horizon radius increases, $\tilde{\eta}$ falls monotonically and asymptotically approaches zero. In this state, the behavior appears more similar to black body radiation. This behavior can be observed for both $\ell > 0$ and $\ell < 0$. It is worth noting that the KR and global monopole parameters affect the decay rate in non-trivial manners. In contrast to the Schwarzschild BH, the sparsity decreases with increasing r_h .

5 Discussions

The comprehensive analyses in the previous sections of the paper aid in understanding the effects of the Lorentz-violating parameter, and more importantly in this regard, the presence of a global monopole charge on the dynamics of spherically symmetric BHs in KR gravity. Since solar system tests indicate that these parameters should be very small, investigating

their nuanced effects on physical properties is of significant interest. To this end, our studies on perturbations of the KR BH with a global monopole charge establish the stability of the BH against perturbations. The analyses show that the QNMs are more sensitive to ℓ than to η ; however, both parameters have distinguishable effects on the QNMs. A comparison of the estimated data with previously reported results for the static non-minimally coupled KR BH [38] shows that the estimated frequencies in this case are lower for all three types of perturbations. Moreover, differences from the GR-Schwarzschild case are subtle, potentially indicating difficulty in possible detection by near-future detectors. The QNMs are estimated with high accuracy using the Padé-averaged WKB method, and the frequency and time-domain results exhibit reasonable agreement. However, it is noted that potential avenues for improvement in the numerical scheme developed for the time-domain analysis remain, including but not limited to using more accurate frequency-extraction approaches such as the matrix-pencil method. In a future study, we aim to obtain more meaningful inferences from BH spectroscopic studies of rotating KR BHs.

Next, the analyses of the effects of the global monopole charge on the greybody bounds yields fascinating results. On separating the spectrum of the KR parameter ℓ into $\ell^- \cup \ell^+$, two different regimes emerged. In particular, analysis in the ℓ^- space showed opposite results to that in the ℓ^+ space. In addition, the results showed that the effect of the multipole moment l remains unchanged when transitioning from the ℓ^- to the ℓ^+ set, implying that the multipole moment no longer interacts with the KR parameter ℓ . In contrast, the variation of the greybody bound is affected by the variation of the global monopole charge in the ℓ^- to ℓ^+ transition.

Lastly, the sparsity of Hawking radiation in light of the influence of the global monopole on the BH in the self-interacting KR field was inspected. The analysis has provided valuable and practical insight into the parameter space. By dividing the possible interval of the KR parameter ℓ into $\ell^- \cup \ell^+$, the results are interpreted from two different points of view. Depending on the positivity (negativity) of ℓ at sufficiently small r_h , the sparsity is found to be lower (higher) than the standard value η_{Sch} , which means that the radiation emitted is less (more) sparse than the Hawking radiation at this stage of evaporation. It was observed that as the radius of the event horizon increases, $\tilde{\eta}$ decreases monotonically and asymptotically approaches zero. In this state, the behavior approximately resembles black body radiation.

References

- [1] LIGO SCIENTIFIC, VIRGO collaboration, *Observation of gravitational waves from a binary black hole merger*, *Phys. Rev. Lett.* **116** (2016) 061102 [[1602.03837](#)].
- [2] T.L.S. Collaboration and the Virgo Collaboration, *Gw151226: Observation of gravitational waves from a 22-solar-mass binary black hole coalescence*, *Phys. Rev. Lett.* **116** (2016) 241103 [[1606.04855](#)].
- [3] EVENT HORIZON TELESCOPE collaboration, *First m87 event horizon telescope results. i. the shadow of the supermassive black hole*, *Astrophys. J. Lett.* **875** (2019) L1 [[1906.11238](#)].
- [4] EVENT HORIZON TELESCOPE collaboration, *First sagittarius a* event horizon telescope results. i. the shadow of the supermassive black hole in the center of the milky way*, *Astrophys. J. Lett.* **930** (2022) L12.
- [5] J. Collins, A. Perez, D. Sudarsky, L. Urrutia and H. Vucetich, *Lorentz invariance and quantum gravity: An additional fine-tuning problem?*, *Phys. Rev. Lett.* **93** (2004) 191301 [[0403053](#)].

- [6] V.A. Kostelecký and S. Samuel, *Spontaneous breaking of lorentz symmetry in string theory*, *Phys. Rev. D* **39** (1989) 683.
- [7] J. Alfaro, H.A. Morales-Tecotl and L.F. Urrutia, *Loop quantum gravity and light propagation*, *Phys. Rev. D* **65** (2002) 103509.
- [8] P. Hořava, *Quantum gravity at a Lifshitz point*, *Phys. Rev. D* **79** (2009) 084008.
- [9] S.M. Carroll, J.A. Harvey, V.A. Kostelecký, C.D. Lane and T. Okamoto, *Noncommutative field theory and lorentz violation*, *Phys. Rev. Lett.* **87** (2001) 141601.
- [10] T. Jacobson and D. Mattingly, *Gravity with a dynamical preferred frame*, *Phys. Rev. D* **64** (2001) 024028.
- [11] S.L. Dubovsky, P.G. Tinyakov and I.I. Tkachev, *Massive graviton as a testable cold-dark-matter candidate*, *Phys. Rev. Lett.* **94** (2005) 181102.
- [12] G.R. Bengochea and R. Ferraro, *Dark torsion as the cosmic speed-up*, *Phys. Rev. D* **79** (2009) 124019.
- [13] A.G. Cohen and S.L. Glashow, *Very special relativity*, *Phys. Rev. Lett.* **97** (2006) 021601.
- [14] V.A. Kostelecký and S. Samuel, *Phenomenological gravitational constraints on strings and higher-dimensional theories*, *Phys. Rev. Lett.* **63** (1989) 224.
- [15] R.V. Maluf and J.C.S. Neves, *Black holes with a cosmological constant in bumblebee gravity*, *Phys. Rev. D* **103** (2021) 044002 [[2011.12841](#)].
- [16] S. Capozziello, S. Zare, D.F. Mota and H. Hassanabadi, *Dark matter spike around bumblebee black holes*, [2303.13554](#).
- [17] M. Khodadi, G. Lambiase and L. Mastrototaro, *Spontaneous lorentz symmetry breaking effects on grbs jets arising from neutrino pair annihilation process near a black hole*, *Eur. Phys. J. C* **83** (2023) 239 [[2302.14200](#)].
- [18] R. Xu, D. Liang and L. Shao, *Bumblebee black holes in light of event horizon telescope observations*, *Astrophys. J.* **945** (2023) 148 [[2302.05671](#)].
- [19] R. Xu, D. Liang and L. Shao, *Static spherical vacuum solutions in the bumblebee gravity model*, *Phys. Rev. D* **107** (2023) 024011 [[2209.02209](#)].
- [20] R. Oliveira, D.M. Dantas and C.A.S. Almeida, *Quasinormal frequencies for a black hole in a bumblebee gravity*, *EPL* **135** (2021) 10003 [[2105.07956](#)].
- [21] F.P. Poulis and M.A.C. Soares, *Exact modifications on a vacuum spacetime due to a gradient bumblebee field at its vacuum expectation value*, *Eur. Phys. J. C* **82** (2022) 613 [[2112.04040](#)].
- [22] R. Casana, A. Cavalcante, F.P. Poulis and E.B. Santos, *Exact schwarzschild-like solution in a bumblebee gravity model*, *Phys. Rev. D* **97** (2018) 104001 [[1711.02273](#)].
- [23] İ. Güllü and A. Övgün, *Schwarzschild-like black hole with a topological defect in bumblebee gravity*, *Annals of Physics* **436** (2022) 168721.
- [24] R. Casana, A. Cavalcante, F. Poulis and E. Santos, *Exact schwarzschild-like solution in a bumblebee gravity model*, *Physical Review D* **97** (2018) 104001.
- [25] A. Övgün, K. Jusufi and I. Sakalli, *Exact traversable wormhole solution in bumblebee gravity*, *Phys. Rev. D* **99** (2019) 024042 [[1804.09911](#)].
- [26] D.J. Gogoi and U.D. Goswami, *Quasinormal modes and hawking radiation sparsity of gup corrected black holes in bumblebee gravity with topological defects*, *Journal of Cosmology and Astroparticle Physics* **2022** (2022) 029.
- [27] M. Kalb and P. Ramond, *Classical direct interstring action*, *Phys. Rev. D* **9** (1974) 2273.

- [28] B. Altschul, Q.G. Bailey and V.A. Kostelecký, *Lorentz violation with an antisymmetric tensor*, *Phys. Rev. D* **81** (2010) 065028 [[0912.4852](#)].
- [29] I. Bandos, K. Lechner, D. Sorokin and P.K. Townsend, *On p-form gauge theories and their conformal limits*, *J. High Energy Phys.* **2021** (2021) 1 [[2012.09286](#)].
- [30] R.M. Wald, *General Relativity*, University of Chicago Press (2010).
- [31] W.F. Kao, W.B. Dai, S.-Y. Wang, T.-K. Chyi and S.-Y. Lin, *Induced einstein-kalb-ramond theory and the black hole*, *Phys. Rev. D* **53** (1996) 2244.
- [32] S. SenGupta and S. Sur, *Spherically symmetric solutions of gravitational field equations in kalb-ramond background*, *Physics Letters B* **521** (2001) 350.
- [33] S. Kar, S. SenGupta and S. Sur, *Static, spherically symmetric solutions, gravitational lensing, and perihelion precession in einstein-kalb-ramond theory*, *Physical Review D* **67** (2003) 044005.
- [34] S. Chakraborty and S. SenGupta, *Strong gravitational lensing—a probe for extra dimensions and kalb-ramond field*, *Journal of Cosmology and Astroparticle Physics* **2017** (2017) 045.
- [35] D. Maity, P. Majumdar and S. SenGupta, *Parity-violating kalb-ramond-maxwell interactions and cmb anisotropy in a braneworld*, *Journal of Cosmology and Astroparticle Physics* **2004** (2004) 005.
- [36] P.S. Letelier, *Spinning strings as torsion line spacetime defects*, *Classical and Quantum Gravity* **12** (1995) 471.
- [37] L.A. Lessa, J.E.G. Silva, R.V. Maluf and C.A.S. Almeida, *Modified black hole solution with a background kalb-ramond field*, *Eur. Phys. J. C* **80** (2020) 1.
- [38] A. Baruah, A. Övgün and A. Deshamukhya, *Quasinormal modes and bounding greybody factors of GUP-corrected black holes in kalb-ramond gravity*, *Ann. Phys.* **455** (2023) 169393.
- [39] F. Atamurotov, D. Ortiqboev, A. Abdujabbarov and G. Mustafa, *Particle dynamics and gravitational weak lensing around black hole in the kalb-ramond gravity*, *The European Physical Journal C* **82** (2022) 659.
- [40] J. Ellis, N.E. Mavromatos and S. Sarkar, *Environmental cpt violation in an expanding universe in string theory*, *Physics Letters B* **725** (2013) 407.
- [41] S. Kar, P. Majumdar, S.S. Gupta and S. Sur, *Cosmic optical activity from an inhomogeneous kalb-ramond field*, *Classical and Quantum Gravity* **19** (2002) 677.
- [42] M. Fathi and A. Övgün, *Black hole with global monopole charge in self-interacting kalb-ramond field*, *arXiv preprint arXiv:2501.09899* (2025) .
- [43] A. Vilenkin, *Gravitational field of vacuum domain walls and strings*, *Physical Review D* **23** (1981) 852.
- [44] A. Vilenkin, *Cosmological evolution of monopoles connected by strings*, *Nuclear Physics B* **196** (1982) 240.
- [45] N. Dadhich, K. Narayan and U. Yajnik, *Schwarzschild black hole with global monopole charge*, *Pramana* **50** (1998) 307.
- [46] M. Barriola and A. Vilenkin, *Gravitational field of a global monopole*, *Phys. Rev. Lett.* **63** (1989) 341.
- [47] K.A. Bronnikov, B.E. Meierovich and E.R. Podolyak, *Global monopole in general relativity*, *Journal of Experimental and Theoretical Physics* **95** (2002) 392.
- [48] K. Yang, Y.-Z. Chen, Z.-Q. Duan and J.-Y. Zhao, *Static and spherically symmetric black holes in gravity with a background kalb-ramond field*, *Phys. Rev. D* **108** (2023) 124004.
- [49] *Proceedings of the Third Marcel Grossmann Meeting on General Relativity*, 1983.

- [50] B.F. Schutz and C.M. Will, *Black hole normal modes: a semianalytic approach*, *Astrophys. J.* **291** (1985) L33.
- [51] S. Iyer and C.M. Will, *Black-hole normal modes: A WKB approach. i. foundations and application of a higher-order WKB analysis of potential-barrier scattering*, *Phys. Rev. D* **35** (1987) 3621.
- [52] R.A. Konoplya, *Quasinormal behavior of the d-dimensional schwarzschild black hole and the higher order wkb approach*, *Phys. Rev. D* **68** (2003) 024018.
- [53] J. Matyjasek and M. Opala, *Quasinormal modes of black holes: The improved semianalytic approach*, *Phys. Rev. D* **96** (2017) 024011.
- [54] R.A. Konoplya and A. Zhidenko, *Quasinormal modes of black holes: From astrophysics to string theory*, *Rev. Mod. Phys.* **83** (2011) 793.
- [55] R.A. Konoplya, A. Zhidenko and A.F. Zinhailo, *Higher order WKB formula for quasinormal modes and grey-body factors: recipes for quick and accurate calculations*, *Class. Quantum Gravity* **36** (2019) 155002.
- [56] M. Bouhmadi-López, S. Brahma, C.-Y. Chen, P. Chen and D.-h. Yeom, *A consistent model of non-singular schwarzschild black hole in loop quantum gravity and its quasinormal modes*, *J. Cosmol. Astropart. Phys.* **2020** (2020) 066.
- [57] S. Chandrasekhar, *Selected Papers, Volume 6: The Mathematical Theory of Black Holes and of Colliding Plane Waves*, vol. 6, University of Chicago Press (1991).
- [58] M. Abramowitz and I.A. Stegun, *Handbook of Mathematical Functions*, vol. 55, Dover, New York (1964).
- [59] C.-Y. Chen and P. Chen, *Gravitational perturbations of nonsingular black holes in conformal gravity*, *Phys. Rev. D* **99** (2019) 104003 [[1902.01678](#)].
- [60] C. Gundlach, R.H. Price and J. Pullin, *Late-time behavior of stellar collapse and explosions. i. linearized perturbations*, *Phys. Rev. D* **49** (1994) 883–889.
- [61] C. Gundlach, R.H. Price and J. Pullin, *Late-time behavior of stellar collapse and explosions. ii. nonlinear evolution*, *Phys. Rev. D* **49** (1994) 890–899.
- [62] E. Berti, V. Cardoso, J.A. Gonzalez and U. Sperhake, *Mining information from binary black hole mergers: a comparison of estimation methods for complex exponentials in noise*, *Physical Review D—Particles, Fields, Gravitation, and Cosmology* **75** (2007) 124017.
- [63] M. Visser, *Some general bounds for 1-d scattering*, *Phys. Rev. A* **59** (1999) 427 [[quant-ph/9901030](#)].
- [64] P. Boonserm and M. Visser, *Bounding the greybody factors for schwarzschild black holes*, *Phys. Rev. D* **78** (2008) 101502 [[0806.2209](#)].
- [65] Y. Yang, D. Liu, A. Övgün, Z.-W. Long and Z. Xu, *Probing hairy black holes caused by gravitational decoupling using quasinormal modes and greybody bounds*, *Phys. Rev. D* **107** (2023) 064042 [[2203.11551](#)].
- [66] F. Gray and M. Visser, *Greybody factors for schwarzschild black holes: Path-ordered exponentials and product integrals*, *Universe* **4** (2018) 93 [[1512.05018](#)].
- [67] T. Ngampitipan and P. Boonserm, *Bounding the greybody factors for non-rotating black holes*, *Int. J. Mod. Phys. D* **22** (2013) 1350058 [[1211.4070](#)].
- [68] A. Chowdhury and N. Banerjee, *Greybody factor and sparsity of hawking radiation from a charged spherical black hole with scalar hair*, *Phys. Lett. B* **805** (2020) 135417 [[2002.03630](#)].
- [69] Y.-G. Miao and Z.-M. Xu, *Hawking radiation of five-dimensional charged black holes with scalar fields*, *Phys. Lett. B* **772** (2017) 542 [[1704.07086](#)].

- [70] Y. Liu, *Hawking temperature and the bound on greybody factors in $d = 4$ double field theory*, *Eur. Phys. J. C* **82** (2022) 1054 [[2201.01279](#)].
- [71] S. Barman, *The hawking effect and the bounds on greybody factor for higher dimensional schwarzschild black holes*, *Eur. Phys. J. C* **80** (2020) 50 [[1907.09228](#)].
- [72] H. Xu and M.-H. Yung, *Black hole evaporation in lovelock gravity with diverse dimensions*, *Phys. Lett. B* **794** (2019) 77 [[1904.06503](#)].
- [73] P. Boonserm, T. Ngampitipan and P. Wongjun, *Greybody factor for black holes in drgt massive gravity*, *Eur. Phys. J. C* **78** (2018) 492 [[1705.03278](#)].
- [74] P. Boonserm, T. Ngampitipan and P. Wongjun, *Greybody factor for black string in drgt massive gravity*, *Eur. Phys. J. C* **79** (2019) 1.
- [75] D.N. Page, *Particle emission rates from a black hole: Massless particles from an uncharged, nonrotating hole*, *Phys. Rev. D* **13** (1976) 198.
- [76] F. Gray, S. Schuster, A. Van-Brunt and M. Visser, *The hawking cascade from a black hole is extremely sparse*, *Class. Quant. Grav.* **33** (2016) 115003 [[1506.03975](#)].
- [77] Y. Sekhmani, B. Hazarika, P. Phukon, A. Landry, S.K. Maurya and J. Rayimbaev, *The d -dimensional charged ads black holes solutions in polytropic dark energy from barrow entropy*, [2410.18247](#).
- [78] Y. Sekhmani, D.J. Gogoi, M. Koussour, R. Myrzakulov and J. Rayimbaev, *Shadows of r -charged black holes in ads5*, *Phys. Dark Univ.* **44** (2024) 101442.